



City Research Online

City St George's, University of London

Citation: Khan, K., Chen, Z., Liu, J. & Tsavdaridis, K. D. (2023). Compressive behaviors of corner-supported modular steel sway frames with rotary inter-modular connections. *Thin-Walled Structures*, 193, 111245. doi: 10.1016/j.tws.2023.111245

This is the accepted version of the paper.

This version of the publication may differ from the final published version. To cite this item please consult the publisher's version.

Permanent repository link: <https://openaccess.city.ac.uk/id/eprint/31773/>

Link to published version: <https://doi.org/10.1016/j.tws.2023.111245>

Copyright and Reuse: Copyright and Moral Rights remain with the author(s) and/or copyright holders. Copies of full items can be used for personal research or study, educational, or not-for-profit purposes without prior permission or charge, unless otherwise indicated, provided that the authors, title and full bibliographic details are credited, a hyperlink and/or URL is given for the original metadata page and the content is not changed in any way. For full details of reuse please refer to [City Research Online policy](#).

Compressive behaviors of corner-supported modular steel sway frames with rotary inter-modular connections

Kashan Khan^a, Zhihua Chen^{a,b,c}, Jiadi Liu^a, Konstantinos Daniel Tsavdaridis^d

^a Department of Civil Engineering, Tianjin University, Tianjin, China

^b State Key Laboratory of Hydraulic Engineering Simulation and Safety, Tianjin, China

^c Key Laboratory of Coast Civil Structure and Safety, Tianjin University, Tianjin, China

^d Department of Engineering, School of Science & Technology, City, University of London, Northampton Square, EC1V 0HB, London, UK

Abstract: Corner-supported modular steel sway frames (CMSFs) with rotary inter-modular connections (IMCs) differed from traditional frames regarding their column discontinuities, beam groupings, and unique intra- and inter-modular connections, necessitating the investigation into their compressive performance to guarantee their safe and reliable application. This study investigated the compressive behavior of CMSFs with rotary IMCs using experimental tests, numerical modeling, and theoretical analysis. Three compression tests were conducted on sub-assembled CMSFs, considering varying floor and ceiling beam stiffnesses. The results showed that all frames experienced lateral sway, with upper columns at lower regions undergoing inward or outward elastic and plastic local buckling. RS1 (RS2) demonstrated 12% (3%) higher strength than RS3, and stiffness increased by 2% for RS1 compared to RS3. Pre- and post-ultimate ductility of RS3 was 3% (13%) and 20% (37%) greater than RS1 (RS2), indicating that increased rigidity with thicker beams enhanced strength and stiffness but resulted in reduced CMSFs' ductility. A finite element model (FEM) was generated, and its accuracy was verified using experimental load-shortening and failure outcomes, revealing an average prediction error of 0.3%, 9.1%, and 8.5% for compressive resistance, stiffness, and ductility index, respectively. Based on validated FEMs, a parametric study was conducted on 77 CMSFs to investigate the effects of varying beam and column sizes, lengths, beam gaps, and connecting plate thicknesses on compressive resistance, stiffness, and pre- and post-ultimate ductilities. Increasing

29 column and beam sizes from 150 to 200 mm and thicknesses from 6 to 8 mm enhanced
30 strength and stiffness by up to 123% (55%) and 46% (10%), with pre-and post-ultimate
31 ductility growing by 16% (113%) and 15% (19%). However, lengthening them from
32 0.6 to 1.2 and 3 m decreased CMSFs' strength (stiffness) by up to 37% (5%) and 65%
33 (71%), with no IMC failure. The sub-assembled CMSFs' buckling load was evaluated
34 using theoretical models, considering members' stiffnesses and rotary IMC as pinned
35 and semi-rigid. The average theory-to-FEM buckling load for pinned and semi-rigid
36 IMC was 0.70 and 0.96, indicating that both models were conservative. However,
37 considering IMC's rotational stiffness provided less scattering and a more realistic
38 depiction of the CMSFs' buckling behavior than the pinned model. The study's findings
39 and the accuracy of theoretical buckling models ensured they could conservatively
40 design CMSFs under compressive loadings while considering their uniquenesses.

41 **Keywords:** Compressive behaviors; Rotary inter-modular connections; Corner-
42 supported modular steel sway frames; Sub-assembled frame testing; Finite element
43 parametric analysis; Theoretical buckling load models

44

45 **1 Introduction**

46 Modular steel buildings (MSBs) utilize prefabricated modules interconnected with
47 inter-modular connections (IMCs) to create efficient, high-quality, safe, and eco-
48 friendly structures [1,2]. They have emerged as successful alternatives to traditional
49 steel buildings (TSBs) for various projects, such as COVID-19 hospitals [3], 29-story
50 SOHO and Apex [4], and 32-story B2 towers [5]. The assembly, structural stability,
51 and performance of MSBs rely significantly on intra- and inter-modular connections.
52 Beam-column intra-modular connections are typically welded joints due to their higher
53 capacity than fin-plate or bolted connections [2]. Meanwhile, IMCs transmit forces
54 between modules [6]. Considerable investigation has been carried out on IMC designs
55 and their mechanical performance under various loading conditions, leading to a
56 comprehensive understanding of their advantages and limitations [4,5,7–11].

57 Corner-supported modular steel units in MSBs provide a distinct load transfer path and
58 superior offsite prefabrication compared to other modules [12,13]. Corner-supported
59 modular steel sway frames (CMSFs), or non-sway frames, have been the primary focus
60 of IMC research, with CMSFs capable of replicating nonlinear P -Delta effects, leading
61 to significant bending moments in intra- and inter-modular connections and distinct
62 structural responses compared to non-sway frames [14]. Extensive research has been
63 conducted on tensile [15–18], shear [17,19–24], bending [21,25,26], and seismic
64 performance [16,27–35] of welded [36–40], bolted [2,26,27,41–47], shear-keyed
65 [24,29,54–63,34,64–71,35,48–53], pre- and post-tensioned [19,20,25,28,31,67,72,73],
66 and automatic [16,18,23,30,50,74–76] IMCs. Depending on load capacity, resilience,
67 installation convenience, and disassembly, each IMC type has pros and cons. For
68 instance, welded IMCs are durable but susceptible to weld fractures or stress
69 concentration [28]. Bolted IMCs are ductile but less resilient than welded joints and

70 require member openings, making them prone to gradual loosening or failure [7].
71 Shear-keyed IMCs are stiff and effective against lateral loads, but they can cause
72 column shear stresses and require careful installation [51,77]. Pre- and post-tensioned
73 IMCs are strong but may experience tension relaxation issues over time and require
74 specialized equipment and expertise for installation [7,17]. Automatic IMCs are
75 resilient and self-tightening but require high precision and are complex to install [30].
76 Besides, the low rotational stiffness of welded or cover-plate bolted IMCs hinders them
77 from being used in high-rise MSB or earthquake-prone regions [33]. The inability to
78 disassemble these IMCs prevents MSB reuse [15]. Rotary IMC eliminates the need for
79 on-site welding or member opening, allowing for fast disassembly and the choice of
80 alternative cross-sectional forms [2,17,26,41,42,78]. The complex design of rotary IMC
81 demands specialized skills for precise alignment and compatibility with other modules,
82 as well as load distribution, durability, and compliance with existing structures and
83 design standards, all of which can affect the compressive behavior, stiffness, capacity,
84 and ductility of the CMSFs depicted in **Figs. 1 and 2**. Understanding these factors is
85 crucial for delivering secure and sustainable MSBs [2,26,41,42].
86 Despite extensive research on MSBs under various loads, existing practices, such as
87 alignment charts [79] and simplified equations [80], may not accurately apply to the
88 compressive design of CMSFs due to the semi-rigidity of IMCs, distinguishing them
89 from regular frame systems in TSBs [81]. In MSBs, IMCs generate discontinuities and
90 groupings of columns, beams, and IMCs, unlike traditional continuous columns
91 attached to beams [82–84]. This distinction can lead to non-conservative or excessively
92 conservative designs, posing stability risks for MSBs [85]. While conventional columns
93 have been extensively studied, the compressive behavior of MSBs requires more
94 attention. Some compressive tests on multi-column walls assumed homogeneous load

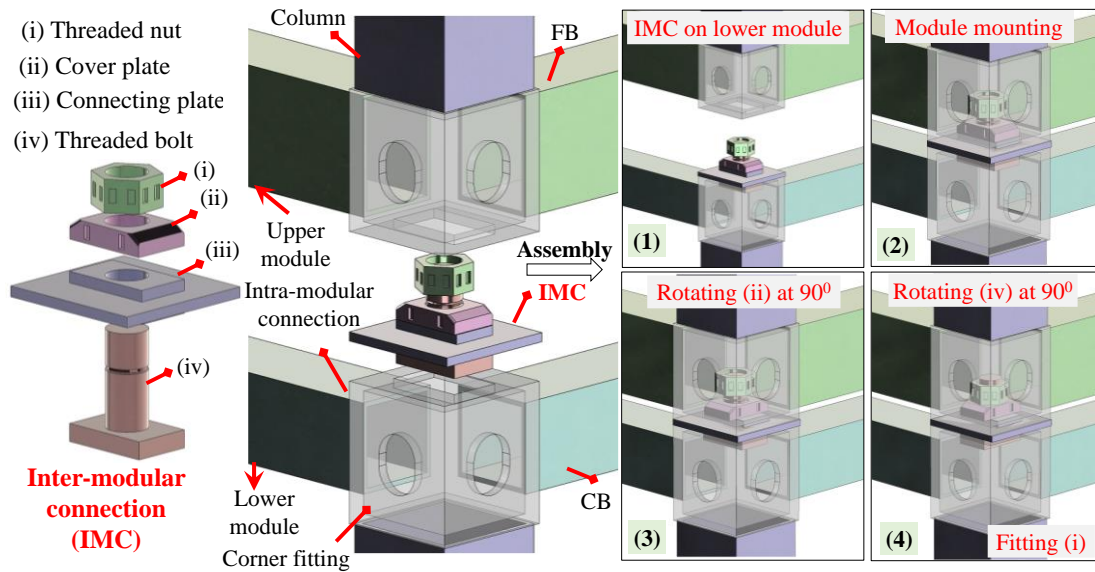
95 distribution and neglected the impact of adjacent modular units, IMCs, and complex
96 joint zones [86–90]. Other studies developed theoretical buckling load models for the
97 conservative design of single and grouped columns with shear-keyed IMCs but did not
98 consider IMCs between adjacent modules [58,63,77,91,92]. A simplified analysis
99 approach to compute column buckling length was proposed by Zhang [93], but its
100 applicability to multi-story MSB columns is unclear. Several focused on stubs or non-
101 sway braced frames with specialized members or IMCs [15,91,92,94–96], but they did
102 not account for the secondary moment effect, limiting their practicality for standard
103 MSBs [97]. Sway and non-sway frames with corner IMCs have been examined by Li
104 et al. [98,99], Farajian et al. [81], Zhai et al. [100], and Wang and Su [101], providing
105 alignment charts for columns K -factors and simplified formulas following French rules
106 [102]. However, these studies lacked experimental support for specific types of IMCs,
107 ignored the rotational stiffness of vertical and horizontal IMCs and joint design, and
108 relied on limited data for fitting, necessitating more precise and straightforward
109 methodologies [100]. Moreover, some studies classified connections' strength and
110 stiffness responses, gave design recommendations, and validated proposed systems, but
111 they disregarded nonlinear analyses and structural post-buckling behavior under
112 multiple limit states [103–105]. Since simplified connections and models cannot
113 accurately determine the structural mechanism, MSB buckling length, and load
114 calculations, they may produce inappropriate values [106]. Assuming rotary IMCs to
115 be either pinned [38,107,108] or rigid [109] in CMSFs, like those used in TSBs
116 [110,111], could lead to inaccurate predictions of the compressive response [15].
117 A comprehensive examination of the compressive behavior of CMSFs considering the
118 P -Delta effect, the relative stiffness of module members and IMCs was needed to
119 develop accurate finite element models (FEMs) for replicating the actual behavior of

120 CMSFs [2,9,82–84,112]. Such analyses were required to focus on the nonlinear
121 behavior of CMSFs. Thus, compressive testing, accurate modeling, analysis, and design
122 were necessary to conservatively evaluate buckling load from semi-rigid to pinned
123 boundaries, eliminating the need for charts to address the shortcomings and ensure the
124 stability, integrity, and resilience of MSBs. Considering the compressive performance
125 of these systems, specific types of IMCs [14], and the stability-relevant mechanical
126 properties of IMCs [2], global stability and reliable design approaches needed to be
127 investigated [106]. The objective of the current study was to contribute to this area by
128 exploring the compressive behavior of CMSFs using rotary IMCs, as outlined in [26].
129 Three subassemblies representing framed exterior modules resembling sway frames
130 were tested under compressive load [14]. Validated FEMs were used to evaluate the
131 effects of parameter variation. The experimental and FEM results corroborated
132 theoretical models assuming semi-rigid and pinned IMCs, enabling conservative
133 predictions of the buckling loads of sub-assembled CMSFs and facilitating the design
134 of cost-effective, secure, and sustainable MSBs.



135 **First formally approved MSB in China, Ziya Shanglinyuan, Tianjin, China**

136 **Fig. 1** Application of CMSFs with rotary IMC patent [113] in authors'
137 designed MSB [114]



138 Rotary IMC installation procedure in corner-supported MSBs (Prototype & Tests)

139 **Fig. 2** Schematic diagram of assembling of CMSF with rotary IMC (IMC's
 140 components design details and specifics based on [2,26,41,42,78])

141 **2 Compression tests on CMSFs with rotary IMCs**

142 Compressive testing of sub-assembled CMSFs with rotary IMCs replicated the exterior
 143 sway frame, examining critical compression stresses that cause stability loss and initiate
 144 buckling.

145 **2.1 Specimens design**

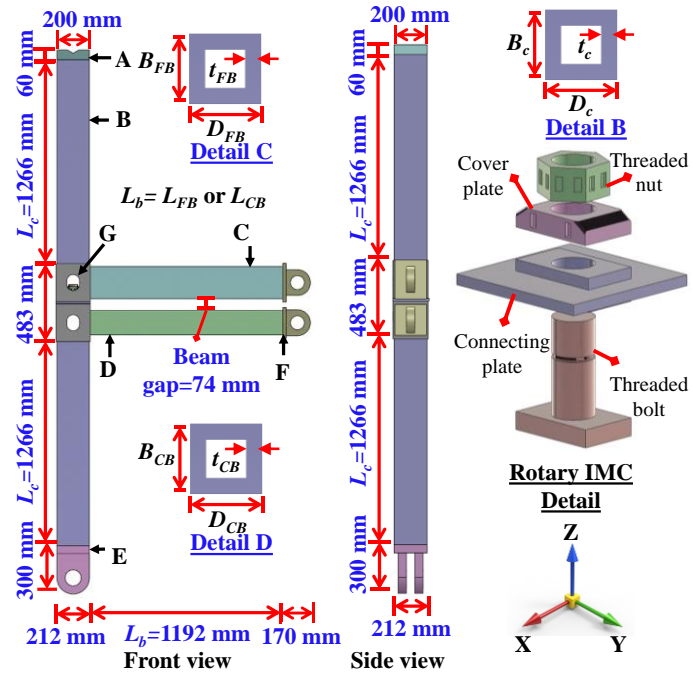
146 **Fig. 1** showed the application of rotary IMC modules in 5-story Ziya Shanglinyuan
 147 MSBs with dimensions of 8.5×3.0×3.0 m and 6.7×3.0×3.0 m [2,17,26,41,42,78] per
 148 GB50017-2017 [115], serving as a prototype for this study's engineering context and
 149 IMC designs. The IMC consisted of four components: a threaded nut, cover plate,
 150 connecting plate, and threaded bolt, whose installation procedures were depicted in **Fig.**
 151 **2**. To examine compressive behavior and failure response in CMSFs, three sub-
 152 assembled exterior frames were designed, each incorporating unique roller supports on
 153 beam ends [14]. The objective of the testing was to gather empirical data for FEM
 154 validation, followed by parametric and theoretical research to develop buckling load
 155 models that incorporate rotary IMCs. The current study adopted sub-assembled
 156 specimens, so the outcomes were related to those in full-frame [14,16,28–31,116]. The

157 lengths of columns and beams were determined using mid-length inflection points,
158 which comprised half of their total lengths. While the semi-rigid behavior of rotary
159 IMCs could affect the CMSF's inflection point, the specimen's design employed
160 simplified pinned-ended assumptions, ignoring IMC rotational rigidity to achieve
161 conservative results by underestimating capacity and stiffness. This offered a
162 comprehensive understanding of the relationship between assumptions and actual
163 behavior, highlighting the significance of joint rigidity when analyzing the compressive
164 behavior of CMSF [14]. The welding seam for the columns and beams was located in
165 the middle of the section, resulting in a butt joint created with groove welding.
166 Following the prototype project, a 74 mm gap was maintained between floor beams
167 (FBs) and ceiling beams (CBs) to allow for services [14].

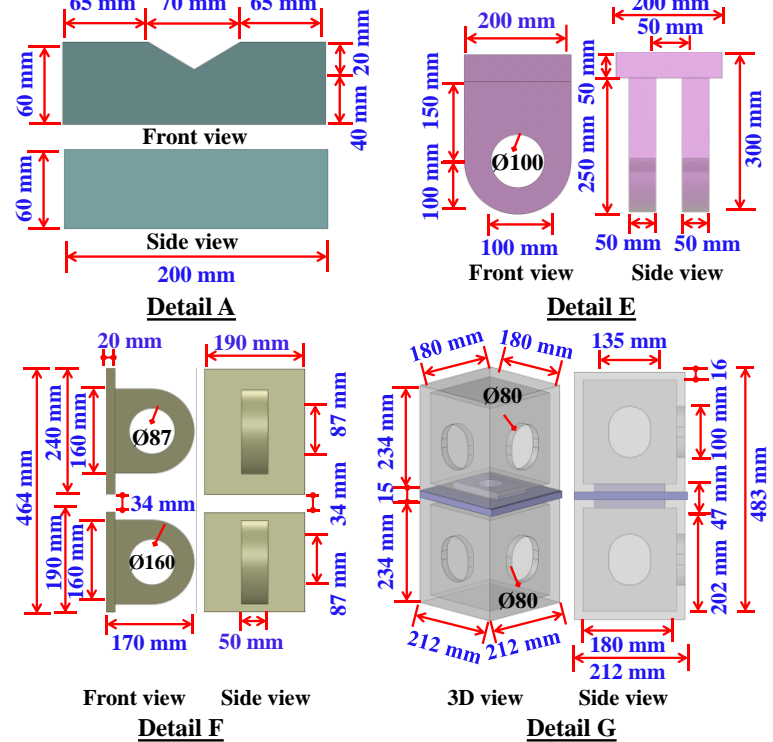
168 **2.2 Specimens geometry**

169 **Fig. 3(a,b)** and **Table 1** presented specimen geometry and component design details,
170 while the IMC components' design details were from previous works [2,26,41,42,78],
171 as depicted in **Fig. 3(c)**. Due to the primary load-bearing member, the flexural stiffness
172 of FBs was maintained higher than that of CBs; therefore, the cross-sectional depth of
173 FBs (B_{FB}) was greater than that of CBs (B_{CB}). RS1 selected a thicker FB than CB,
174 whereas RS2 and RS3 selected similar thicknesses [116]. The thickness of the ceiling
175 beam (t_{CB}) was increased to 8 mm in RS2, and the thickness of the floor beam (t_{FB}) was
176 decreased to 6 mm in RS3 relative to RS1. Various t_{FB} and t_{CB} were considered to
177 examine the effect of beam and intra-modular connections on the compressive
178 behaviors of CMSFs. All specimens were prepared with identical heights and widths of
179 3375 and 1568 mm while maintaining the clear height and length of the upper and lower
180 columns (L_c) at 1266 mm, and the floor (L_{FB}) and ceiling (L_{CB}) beams at 1192 mm.
181 Adopted was the same 200×200×8 mm column measuring 200 mm in length (D_c), 200

182 mm in width (B_c), and 8 mm in thickness (t_c). Cross-section width (D_{FB}) and depth (B_{FB})
 183 of 150 and 200 mm for FBs and width (D_{CB}) and depth (B_{CB}) of 150 mm for CBs were
 184 selected. Meanwhile, members' cross-section sizes, columns height, and beam lengths
 185 (L_c , L_{FB} , and L_{CB}) were maintained.



(a) Specimen details of CMSF with rotary IMC

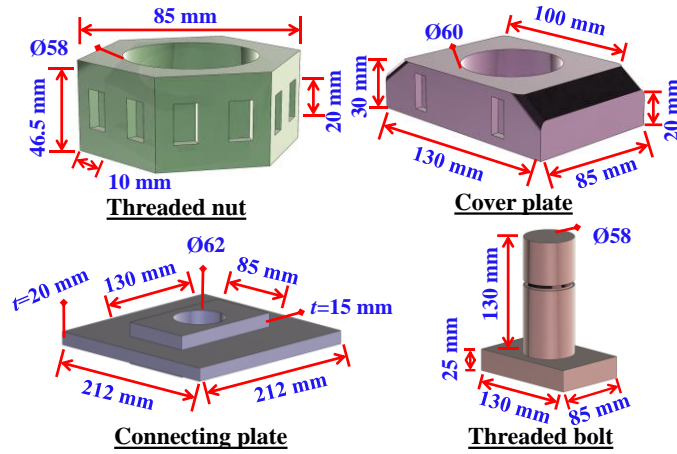


(b) Details of the selected components

186

187

188



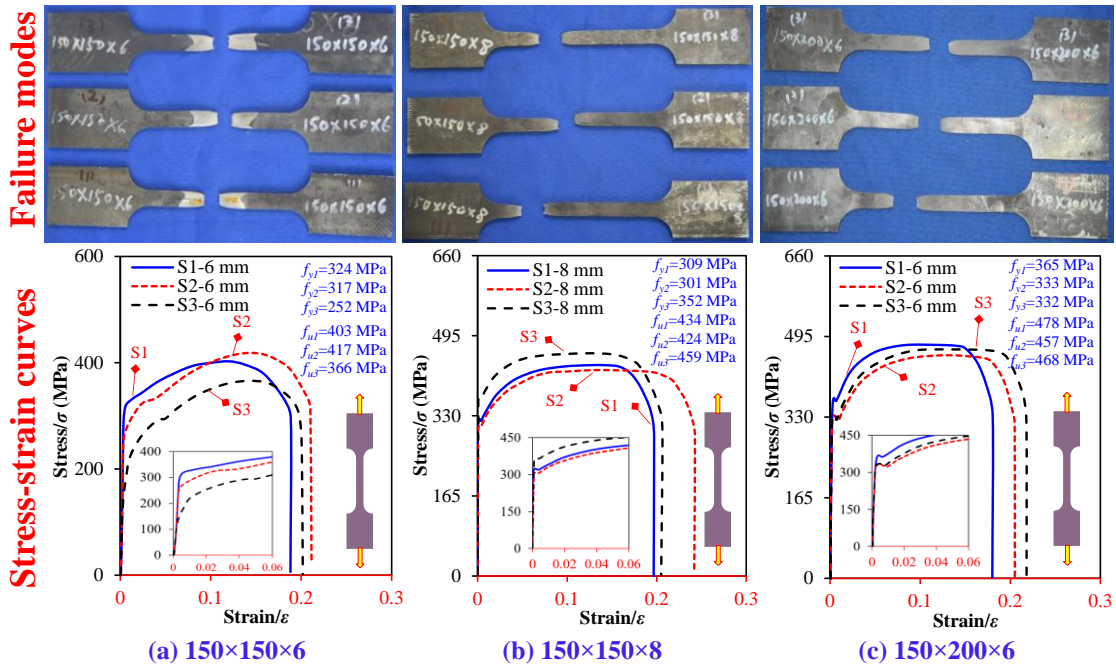
(c) Rotary IMC's components design details

Fig. 3 Details of tested sub-assembled CMSFs with rotary IMCs

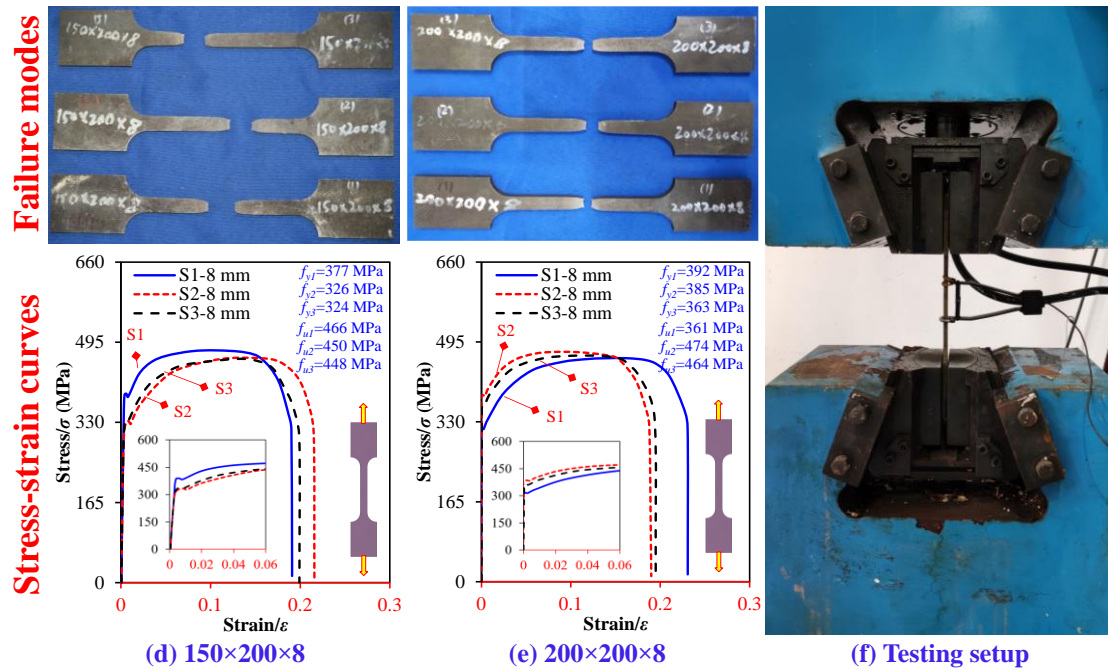
189
190

2.3 Material properties

191 GB/T228.1-2010 [117] was used to design steel coupons from the same material to
 192 analyze test results and generate FEM. Thickness measurements of 15 coupons, three
 193 for each of the five cross-sectional sizes of members, showed variations that notably
 194 affected strength, ductility, failure modes, and yield plateau, while stiffness remained
 195 constant. The mean values of the obtained parameters and thicknesses are detailed in
 196 Table 1. Additionally, Fig. 4(a-f) illustrates the test setup, failure modes, and tensile
 197 stress-strain curves of the coupons.
 198



199



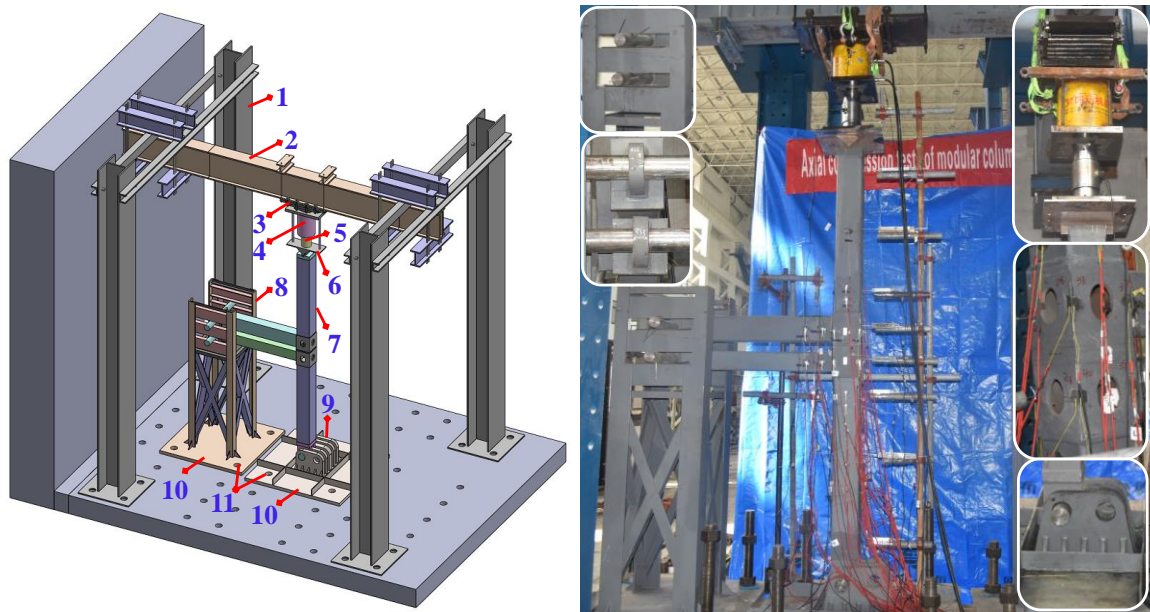
200
201 **Fig. 4** Coupons' tensile testings outcomes

202 **2.4 Test setup**

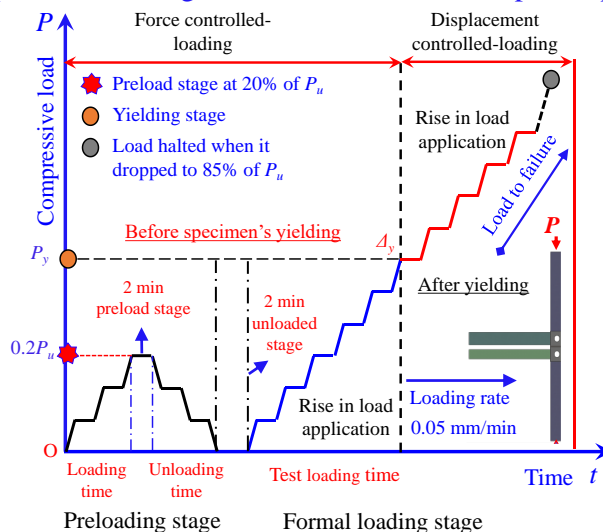
203 **Fig. 5(a,b)** depicts the CMSF's compression testing setup. The specimens' upper and
 204 lower frame skeletons were connected with rotary IMC on the ground, as illustrated in
 205 **Fig. 2**, before being mounted on the setup following [2,17,26,41,42,78]. A 300t vertical
 206 hydraulic jack applied compressive force to the upper columns. Column roller supports
 207 were positioned above the jack to facilitate lateral movement of the jack and specimen,
 208 maintaining compressive force even during specimen shortening and lateral deflection.
 209 The jack's base was secured to a load sensor using a plate and threaded bolts to record
 210 reaction forces. The load sensor's top and bottom ends were anchored with a jack and
 211 knife-edge support through threaded bolts welded onto plates. The knife-edge support
 212 was welded to the bottom end of the plate to maintain flat support, transferring load
 213 instantly to the upper column while allowing rotation. This support enabled in-plane
 214 rotation while restricting out-of-plane rotation. On the ends of beams, roller supports
 215 were devised and installed to limit vertical translation while allowing lateral translation
 216 and in-plane rotation. At the lower column's base, a pin cell provided hinged support,

217 preventing in- and out-of-plane translation while allowing in-plane rotation. As a
218 standard for column-end loadings, a similar testing technique was recommended in [14],
219 as seen in [2,28,29,31,34,41,42,78,118]. A laser level was used to verify the specimen
220 and load setup's straightness. Afterward, the jack was slightly pressed to maintain
221 vertical alignment, measuring devices were attached, and formal testing was initiated.
222 The loading was subdivided into preloading and formal loading, as per GB/T50344-
223 2019 [119]. The measuring devices' accuracy was confirmed by applying a $0.2P_u$
224 (CMSF's ultimate compressive resistance) preload. Specimens were held for two
225 minutes after reaching preload before being completely unloaded for another two
226 minutes, as depicted in **Fig. 5(c)** [120,121]. A combination of force and displacement-
227 controlled loadings was adopted, suitable for structures with unpredictable yield
228 displacements [122]. After a force loading till yielding, displacement loading of 0.05
229 mm/min was used until it dropped to 85% of P_u [123]. Once the load-shortening curves
230 entered the nonlinear phase, displacement loading was initiated, determined by reaction
231 forces registered by the load sensor and vertical shortening by LVDT.
232 Strain gauges assess deformation and force transfer mechanisms [124]. As depicted in
233 **Fig. 6(a-c)**, strain gauges were mounted on upper columns (UCs), lower columns (LCs),
234 FBs, CBs, and upper and lower corner fittings to evaluate local elastic or plastic
235 buckling if it happened before or after material's yield [125]. At least one strain gauge
236 was placed in potentially buckling-prone locations to ensure accurate assessment.
237 Columns were susceptible to in- and out-of-plane local buckling near IMC; strain
238 gauges on columns and corner fittings were positioned vertically along the height.
239 Beams were allowed to rotate, and due to significant stress near the intra- and inter-
240 modular connections, strain gauges were placed up to 200 mm. While the FB and CB
241 gap was small for working, no strain gauge was employed there. On RS1, there were

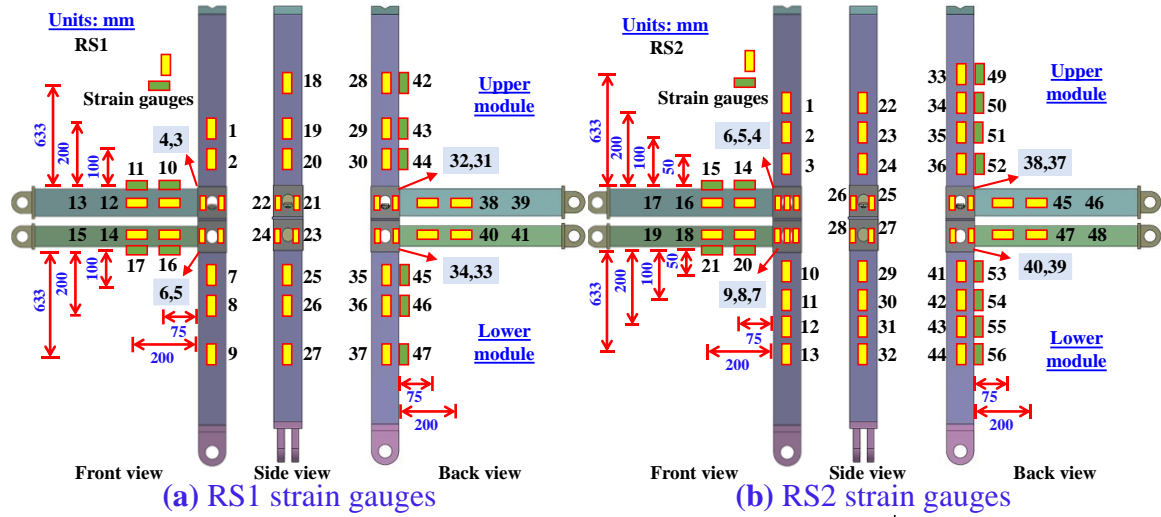
242 47, while on RS2 and RS3, there were 56 strain gauges. As illustrated in **Fig. 6(d)**, eight
 243 horizontal linear variable differential transducers (LVDTs) were positioned vertically
 244 on LCs, UCs, and corner fittings identified by H1-H8 to measure the degree of lateral
 245 deflection, translation, sway, or buckling. A vertical LVDT V3 was mounted on a jack-
 246 fixed knife-edge support to assess the specimens' end-shortening. Similarly, V1 and V2
 247 measured the vertical deflection of CBs and FBs near IMC.



248 (a) Test setup schematic diagram (b) Test setup and specimen before the test



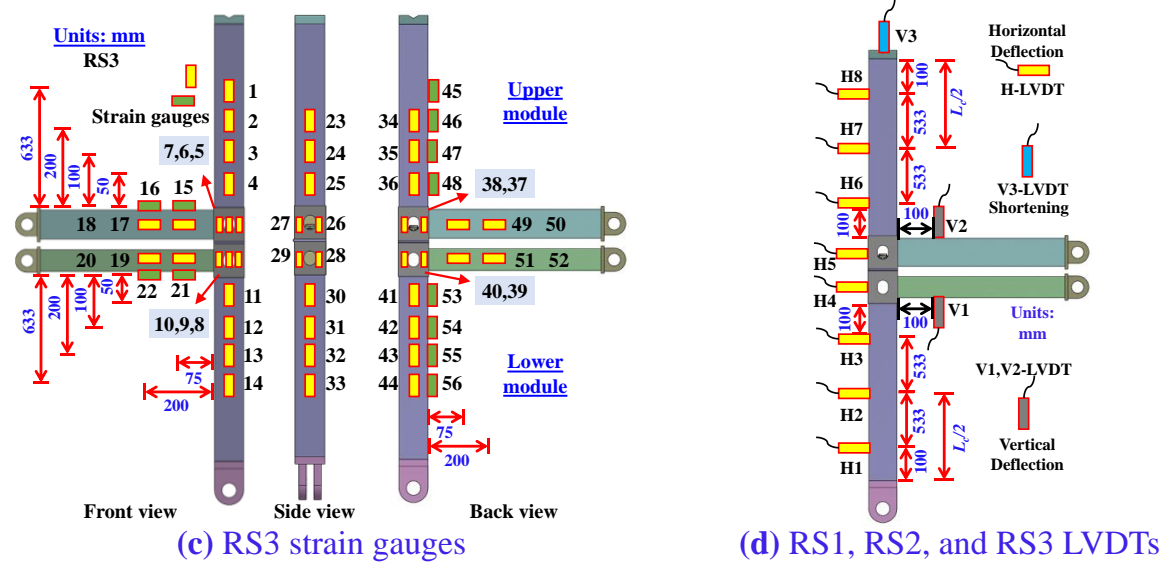
249 (c) Loading protocol
 250 **Fig. 5** Generalized compression testing setup of sub-assembled CMSFs with rotary
 251 IMCs. (1-Reaction frame; 2-Reaction beam; 3-Column roller support; 4; Vertical
 252 hydraulic jack; 5-Load sensor; 6-Knife-edge support; 7; CMSFs specimen with rotary
 253 IMCs; 8-Beams roller support; 9-Hinged support; 10-Pedestal; 11-Anchor bolt holes)



254

(a) RS1 strain gauges

(b) RS2 strain gauges



255

(c) RS3 strain gauges

(d) RS1, RS2, and RS3 LVDTs

Fig. 6 Detailed location of strain gauges and LVDTs on CMSFs

257 **3 Experiment outcomes**

258 **3.1 Failure modes**

259 **Fig. 7(a~c)** demonstrates the CMSF failure mechanisms detected in RS1, RS2, and RS3.

260 As the lateral sway (L_c) indicated, all CMSFs exhibited in-plane translation, controlled

261 by the horizontal translation of floor and ceiling beams, leading to frame instability in

262 the same direction. While all CMSFs experienced the same failure, RS1 and RS3

263 swayed in the direction of beams due to thinner beams compared to columns, but RS2

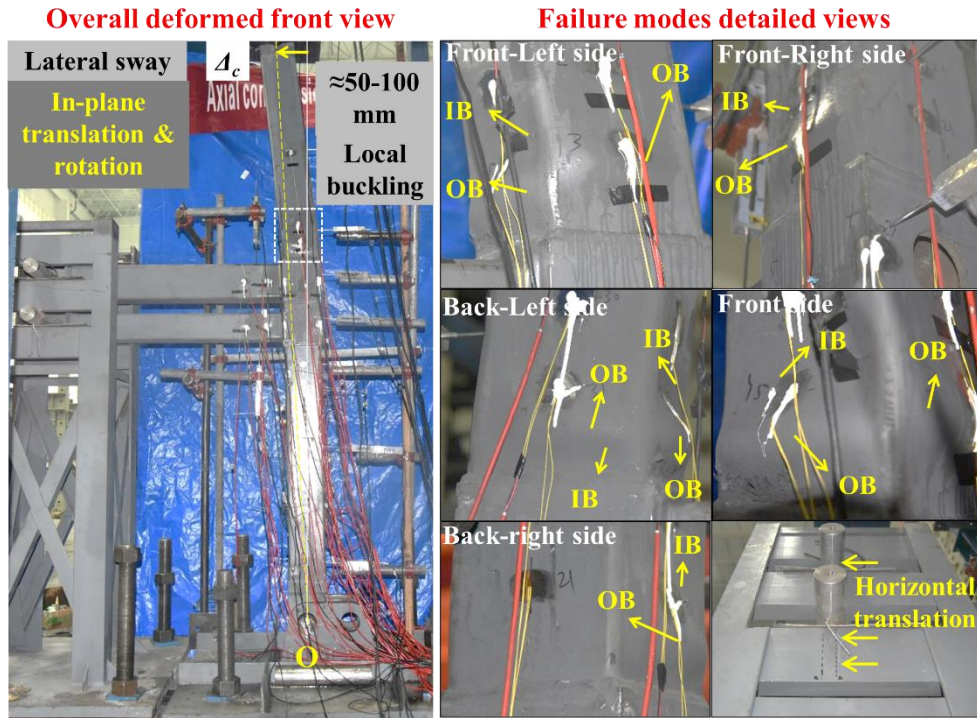
264 exhibited failure in the opposite direction because beams and columns had the same

265 thickness, preventing significant movement towards the beams. The CMSFs displayed

266 distinct translations when subjected to compressive loads, particularly in the FBs and

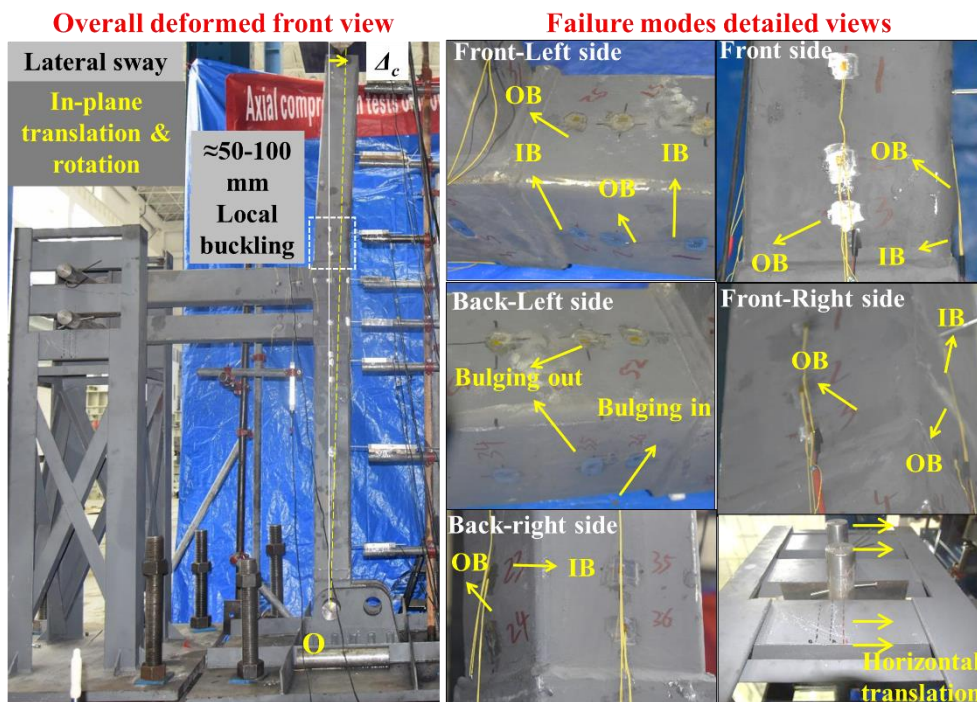
267 CBs. As the applied load increased, lateral translation became more pronounced. While
268 both beams moved in the same direction, there were noticeable variations, especially in
269 the deflection of FBs. For instance, the deflection of FBs increased by 12% in RS1, 16%
270 in RS2, and 15% in RS3. This indicates a significant increase in the in-plane translation
271 of the CMSFs, especially with local column buckling. Additionally, the CB and FB
272 translations were measured at nearly 16 mm and 18 mm in RS1, but these decreased by
273 33% and 31% in RS2 and increased to 79% and 81% for RS3. This suggests that the
274 beams in RS3 demonstrated a more pronounced lateral movement than those in RS1
275 and RS2, highlighting the significant influence of the beams' flexural rigidity on the
276 failure position by affecting stress propagation, translation, and rotation. Moreover,
277 non-rigid constraints permitted the upper and lower frame skeleton's slight gapping and
278 rotation around the IMC. When local buckling occurred in the UC, the CMSF suffered
279 an abrupt rise in in-plane translation. Because the CMSF could not sustain or transfer
280 additional loads after buckling, the loading was halted for safety concerns. Local inward
281 and outward buckling (IB/OB) at the base of the UC towards the IMC was the primary
282 cause of failure. It occurred at a distance of 50-100 mm for RS1 and RS2 while 50-200
283 mm for RS3 from the edge of the corner fitting, confirmed by the greater strain values
284 in the UCs' lower regions. Buckling on the UCs bending side was more apparent than
285 on the opposite. Similar failure modes and their concentration on column faces adjacent
286 to column bending sides supported the absence of out-of-plane translation and rotation,
287 indicating compressive behavior was controlled in-plane. Rotary IMC transmitted force
288 to other members without localized failure, ensuring CMSF's safety and integrity. As
289 shown in **Fig. 11(a~c)**, comparing yield strain showed no location on beams or corner
290 fittings yielded or buckled before achieving CMSF's ultimate compressive resistance.
291 Similarly, most regions on the LCs did not yield; however, several areas on the UCs

292 did yield, indicating that the upper column was the primary load carrier. Except for
 293 portions in or opposite bending directions revealing local elastic buckling, other regions
 294 of UCs exhibited local plastic buckling in CMSFs.



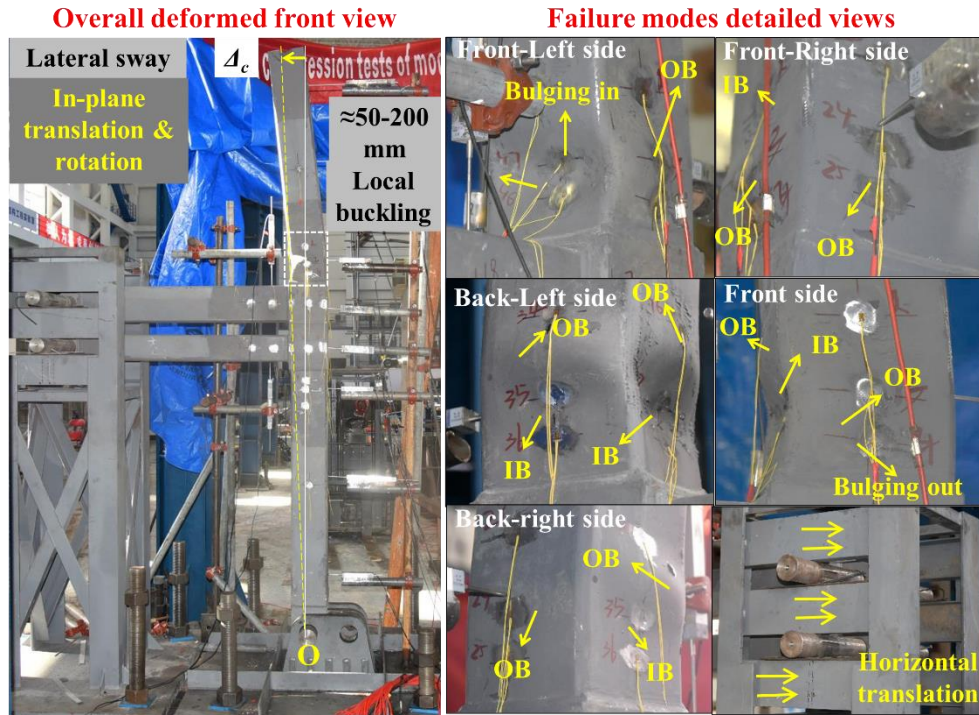
(a) RS1 specimen

295



(b) RS2 specimen

296



(c) RS3 specimen

297
298 **Fig. 7** Failure modes of CMSF under compression (IB/OB, inward/outward buckling)

Table 1 Design details and comparison of compression tests and FEMs of CMSFs with rotary IMC

Item	D_{FB} (mm)	B_{FB} (mm)	t_{FB} (mm)	L_{FB} (m)	D_{CB} (mm)	B_{CB} (mm)	t_{CB} (mm)	L_{CB} (m)	$P_{u,Test}$ (kN)	$K_{e,Test}$ (kN/mm)	$\Delta_{u,Test}$ (mm)	DI_{Test} (Ratio)
RS1	150	200	8	1.2	150	150	6	1.2	1397	343	6.1	1.8
RS2	150	200	8	1.2	150	150	8	1.2	1279	321	5.4	1.4
RS3	150	200	6	1.2	150	150	6	1.2	1244	339	6.2	2.3
Item	$P_{u,Test}$ (kN)	$P_{u,FE}$ (kN)	$\frac{P_{u,Test}}{P_{u,FE}}$	$K_{e,Test}$ (kN/mm)	$K_{e,FE}$ (kN/mm)	$\frac{K_{e,Test}}{K_{e,FE}}$	$\Delta_{u,Test}$ (mm)	$\Delta_{u,FE}$ (mm)	$\frac{\Delta_{u,Test}}{\Delta_{u,FE}}$	DI_{Test} (Ratio)	DI_{FE} (Ratio)	$\frac{DI_{Test}}{DI_{FE}}$
RS1	1397	1403	1.00	343	413	0.83	6.1	4.0	1.53	1.8	2.0	0.94
RS2	1279	1256	1.02	321	342	0.94	5.4	4.6	1.17	1.4	2.0	0.70
RS3	1244	1251	0.99	339	354	0.96	6.2	4.6	1.34	2.3	2.1	1.10
Mean			1.00			0.91			1.35			0.91
Cov			0.01			0.06			0.11			0.18
Item	Length (mm)	Width (mm)	Thickness (mm)	f_y (MPa)	f_u (MPa)	δ (%)	E_s (GPa)					
Beam-1	150	150	6(5.37)	298	395	22.2	201					
Beam-2	150	150	8(7.33)	321	439	23.6	209					
Beam-3	150	200	6(5.54)	344	468	24.9	208					
Beam-4	150	200	8(7.30)	342	455	23.5	210					
Column	200	200	8(7.34)	380	434	22.7	206					
Corner fittings ¹	-	-	16(15.80)	351	518	23.0	198					
IMC (ii, iii) ¹	-	-	-	360	580	34.0	206					
IMC (i, iv) ¹	-	-	-	360	610	16.0	206					

D_{FB} , B_{FB} , t_{FB} , L_{FB} ; D_{CB} , B_{CB} , t_{CB} , L_{CB} ; $P_{u, Test}$ ($P_{u, FE}$), $K_{e, Test}$ ($K_{e, FE}$), $\Delta_{u, Test}$ ($\Delta_{u, FE}$), DI_{Test} (DI_{FE}); and f_y , f_u , δ , E_s represent the floor and ceiling beam's width, depth, thickness, length; ultimate compressive resistance, initial stiffness, ultimate shortening, post-ultimate ductility index via test (FEM); material yield strength, ultimate strength, percentage elongation, elastic modulus—Note:¹ Material properties obtained from [2]. The thickness values in the bracket represent the average measured thickness.

299 3.2 Load-shortening curves

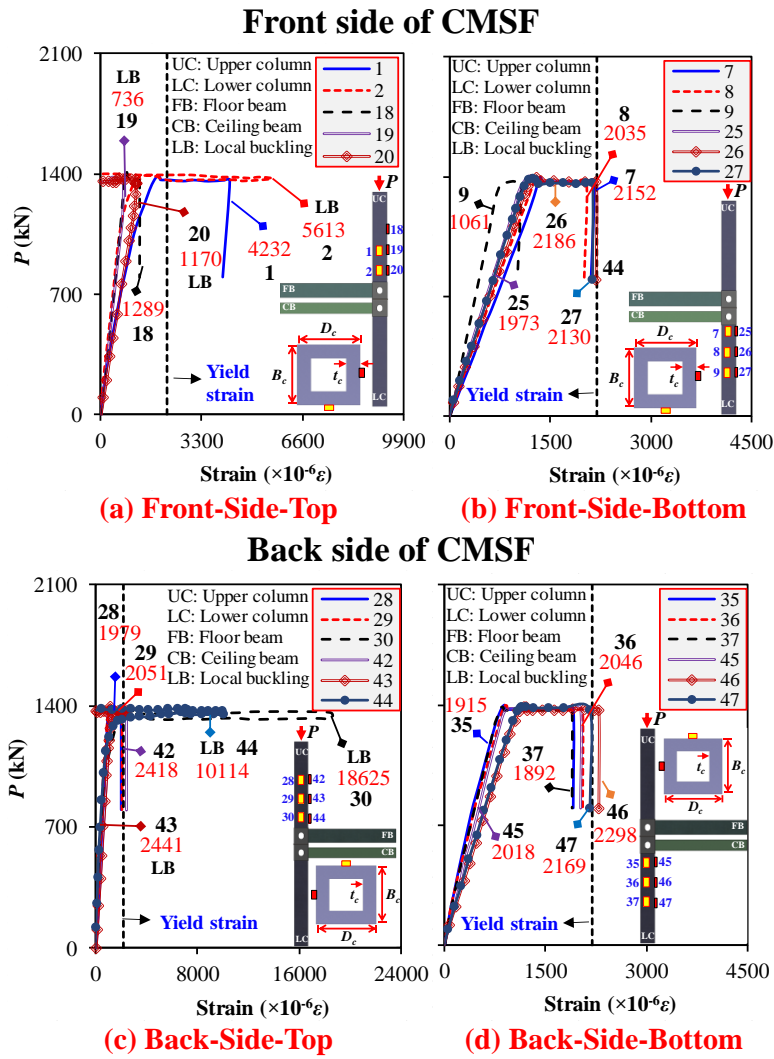
300 **Fig. 17(a~c)** demonstrates the CMSFs' load-shortening ($P-\Delta$) curves, while **Fig. 17(f)**
301 shows their generalized behavior, implying that all illustrations displayed elastic (I),
302 inelastic (II), and recession (III). ' P ' represents the compressive load, while ' Δ ' indicates
303 the shortening. The recession is a stage after the ultimate stage defined by a succeeding
304 trough with a sharp decline in the load-carrying capacity that may extend to larger
305 shortening [126–132]. These curves determine P_u , ultimate shortening (Δ_u), initial
306 stiffness (K_e), and ductility index (DI) [133,134]. The load grows linearly with
307 shortening during stage I until the yield strength (P_y) is achieved. At the transition, the
308 increase in capacity is characterized by a decrease in the stiffness of curves because of
309 exceeding the bending stresses at UCs' multiple locations. During stage II, from P_y until
310 P_u , the curves acquire a parabolic shape; concurrently, local buckling appears on the
311 UCs as an inward and outward pattern as the bending and P -Delta effect intensifies.
312 RS1 (RS2)'s P_u values are 12% (3%) higher than RS3. Compared to RS3, K_e shows
313 marginal fluctuation by rising to 2% for RS1. It indicates that increased rigidity with
314 thicker beams enhances strength and stiffness. Meantime, as determined by strain
315 values, local elastic buckling is found mainly in the bending direction, owing to bending
316 stresses and P -Delta effects that appear to reduce column stiffness relative to other sides.
317 Δ_u of RS3 is 3% (13%) greater than RS1 (RS2) due to the thinner beams, with RS2
318 having the lowest value due to the thickest beams. Thicker beams reduce buckling strain
319 and premature instability, diminishing CMSFs' ductility. Stage III is marked by
320 decreased capacity, sharp deflection increase, and severe local buckling. Similarly, the
321 DI can be compared at the post-ultimate stage. The DI represents the capacity of frame
322 columns to undergo plastic deformation beyond the ultimate load, providing insight
323 into their post-peak deformation capacity, structural stability, and the potential for

324 design improvements and strengthening techniques [77,91,92,123,133]. RS3 has more
325 excellent post-ultimate ductility of 20% (37%) and a better recession stage than RS1
326 (RS2), indicating that stiffer beams enable plastic deformation and improve the
327 structure's ductility index by limiting stress transmission to other components.

328 **3.3 Load-strain curves**

329 **Figs. 8(a~d), 9(a~h), and 10(a~h)** depict load-strain curves and magnitudes on UCs
330 and LCs, highlighting the strain amount, yield strain, and local buckling sites, while
331 **Fig. 11(a~c)** shows the part-wise maximum absolute strain distribution on corner
332 fittings, UCs, LCs, FBs, and CBs. The curves exhibit linear, nonlinear, and recession
333 sections. As load increases, stress rises until local buckling is indicated by inversion,
334 overturning, or abrupt decline in strain curves with exceptionally high values. Curves
335 overturning before or near yield strain signify stresses below the yield strength, causing
336 elastic buckling. Conversely, plastic buckling occurs with stresses surpassing yield.
337 Post-yield overturning curves during the recession phase indicate severe local plastic
338 buckling. Inward and outward buckling occurs in the upper column's lower region,
339 while other members lack buckling or yielding, as indicated by lower strain values in
340 upper and lower corner fittings, highlighting the absence of localized deformation in
341 rotary IMCs. For instance, locations 2, 19, 20, 30, 43, and 44 in RS1, locations 2, 3, 24,
342 36, 50, 51, and 52 in RS2, and locations 2, 3, 4, 23, 24, 25, 34, 35, 46, and 47 in RS3
343 demonstrate the existence of local buckling on each face of UCs lower regions, which
344 exhibits elastic and plastic local buckling. Portions of UCs experiencing bending
345 stresses in or opposite directions of beams display elastic buckling. In contrast, adjacent
346 sides of UCs not exposed to bending undergo plastic buckling. For instance, 19, 20, 43,
347 and 44 in RS1, 50, 51, and 52 in RS2, and 23, 24, and 25 in RS3 display local elastic
348 buckling, suggesting that bending and the *P*-Delta effect prevent UCs and other

349 members from yielding fully. This reveals that the CMSFs' instability is mainly driven
 350 by geometric instability, as opposed to IMCs or members' strength failure.



351

352
 353

Fig. 8 Load-strain curves at columns of RS1

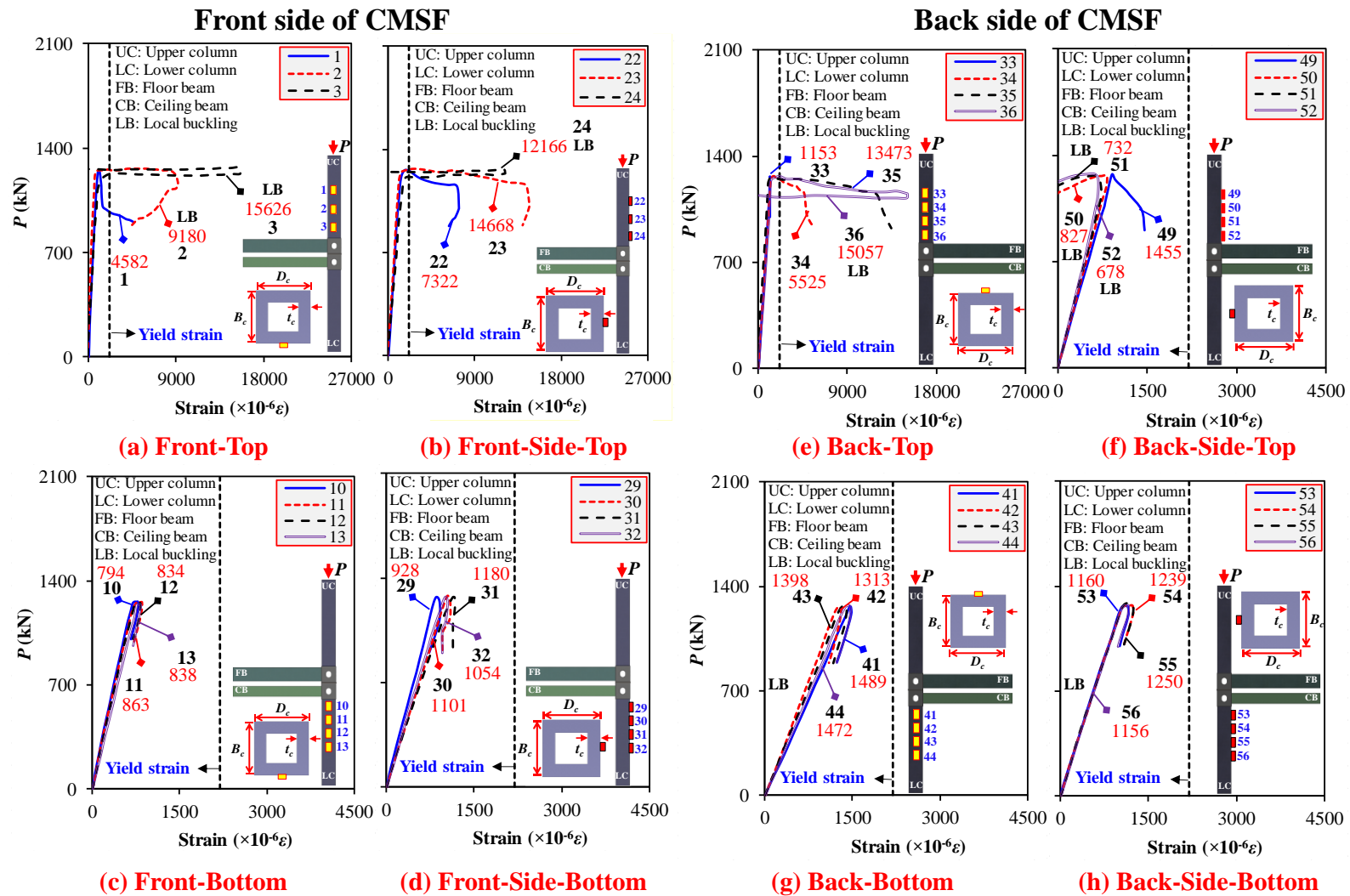


Fig. 9 Load-strain curves at columns of RS2

354
355

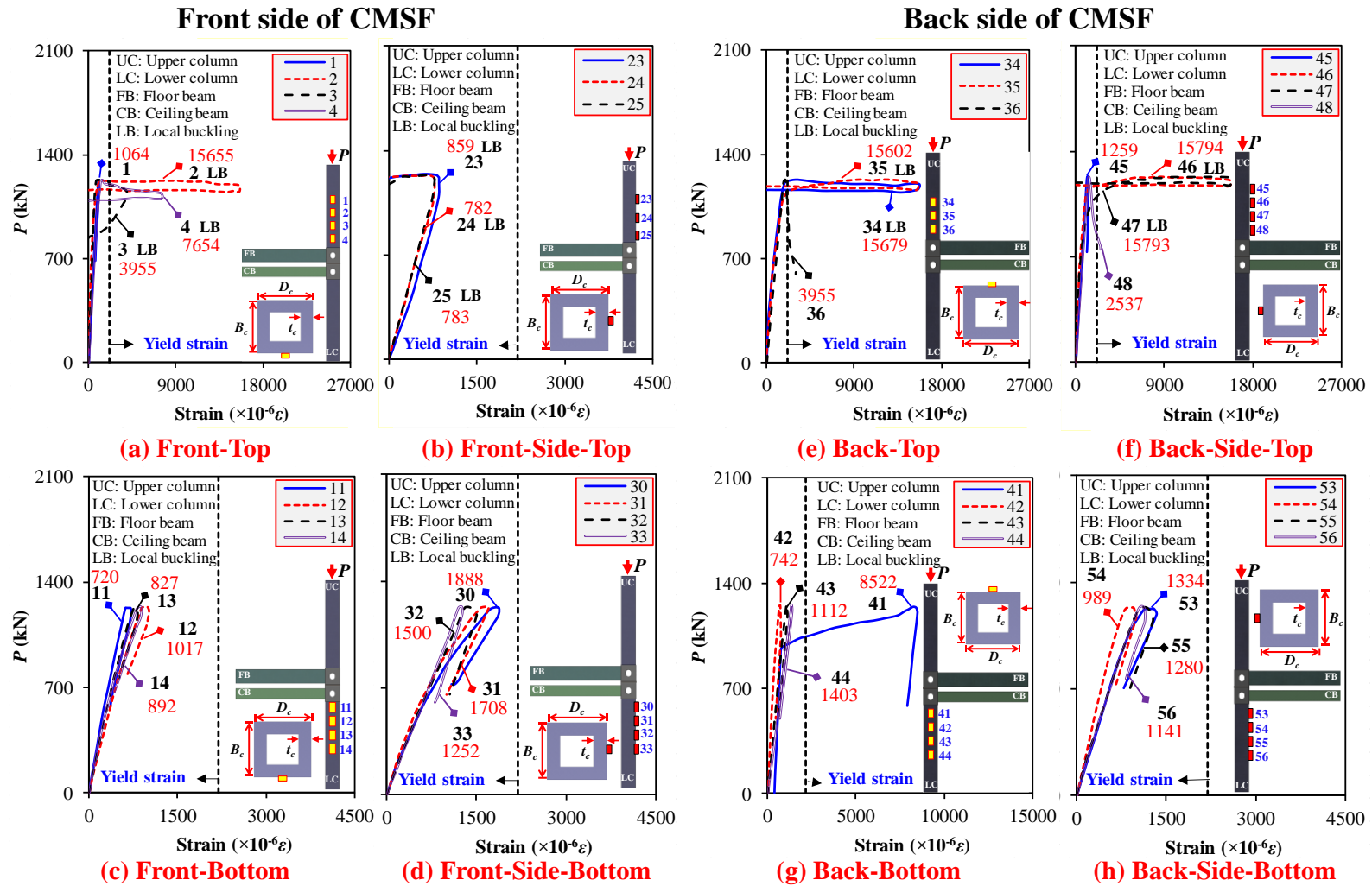
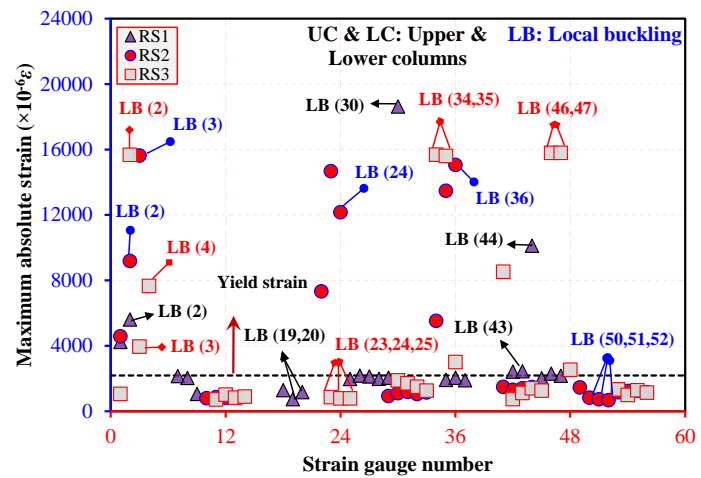
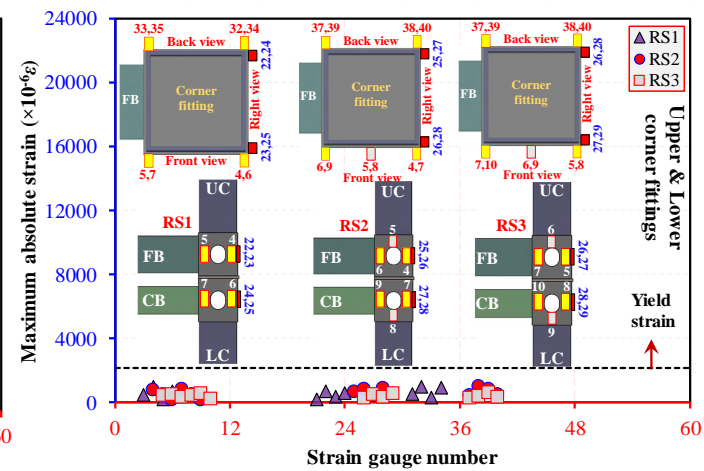


Fig. 10 Load-strain curves at columns of RS3

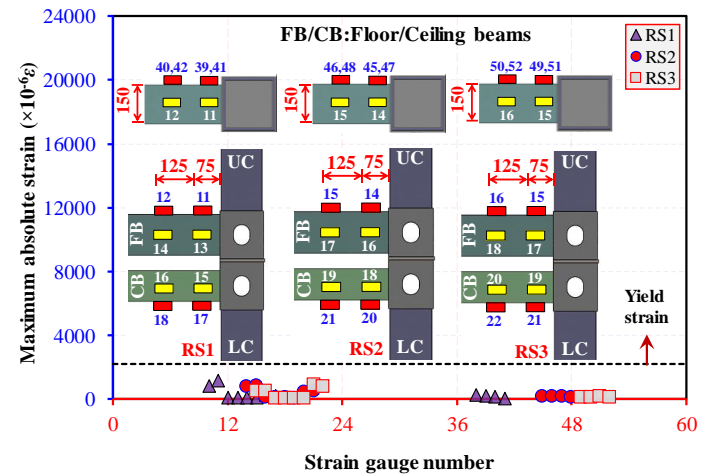
356
357
358



(a) Upper and lower columns



(b) Upper and lower corner fittings



(c) Floor and ceiling beams

Fig. 11 Part-wise maximum absolute strain distribution

359
360

361 3.4 Load-deflection curves

362 **Fig. 12(a~f)** shows the load-deflection curves where the compressive load is denoted
363 by P , and δ signifies the lateral deflection of the columns and the vertical and lateral
364 deflections of the beams. They operate with linear and nonlinear stages, with a lengthy
365 recession phase followed by a curve drop. This is because the failure of CMSFs is
366 limited to bending and local buckling of UCs with sway. While the load increases, the
367 deflection also rises, stabilizing when the ultimate capacity is reached, followed by a
368 pause in load but deflection increments. The orderly increase in lateral deflection from
369 LCs to UCs indicates the presence of CMSF sway, denoted by Δ_c . Simultaneously, the
370 maximum deflection at the top of the UCs suggests CMSFs' instability due to local and
371 global failure. Alternatively, non-identical deflections of FBs and CBs in vertical and
372 lateral directions and their difference imply a degree of relative rotation between the
373 upper and lower frame skeleton at IMCs, which cannot be simulated as rigid or pinned
374 [30]. The varied stiffness decrement of each curve reveals that members act differently
375 with the secondary moment amount they experience. RS3 exhibited a more notable
376 nonlinear stage followed by more significant deflection than RS1 and RS2, indicating
377 that less rigid beams translate more, enhancing CMSF flexibility and force distribution
378 among members. The deflection curve supports test failure modes. Notably, the
379 deflection difference between UC ends (H8 and H6) suggests local buckling initiation
380 near H6, followed by increased top lateral deflection.

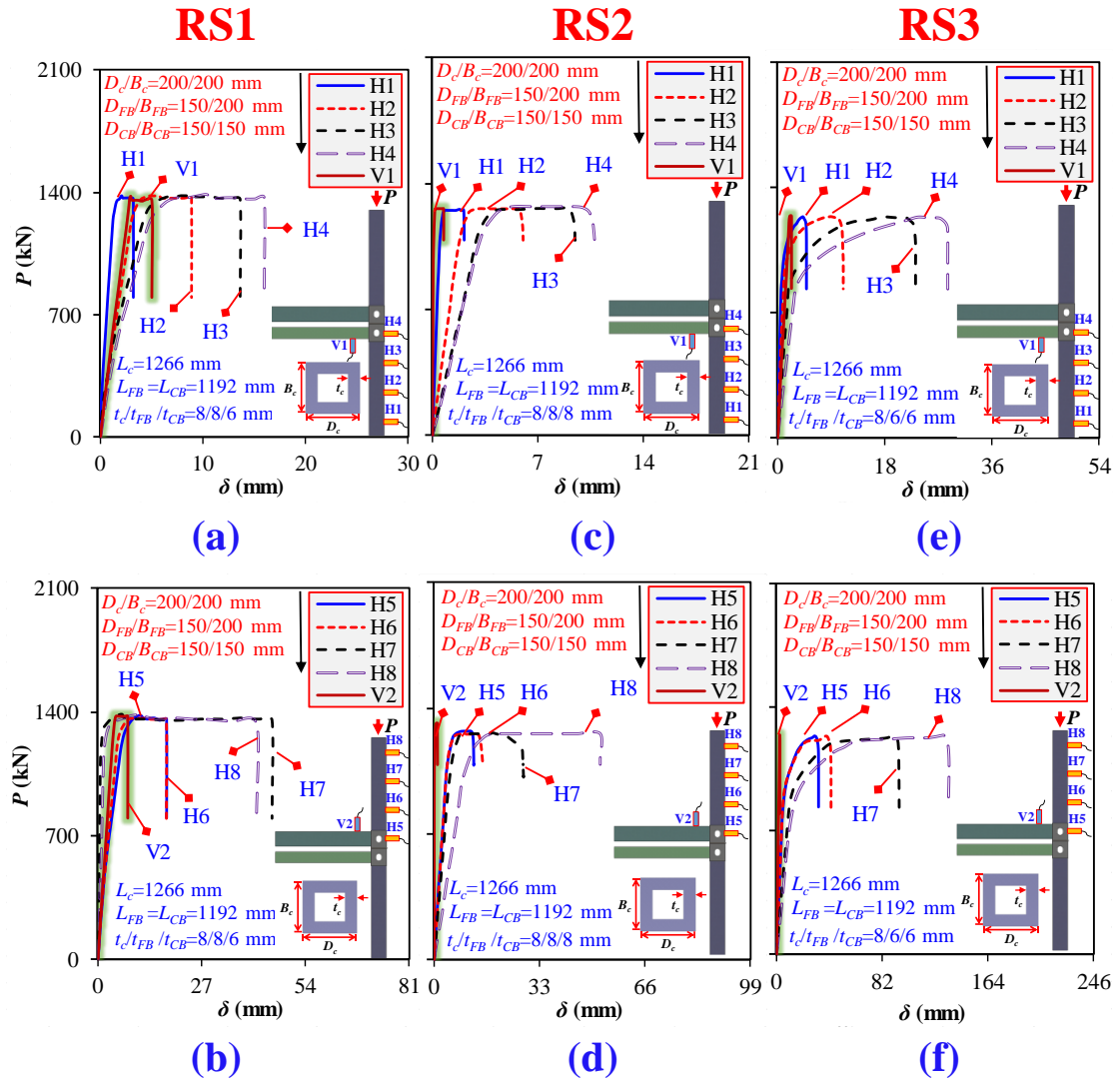


Fig. 12 Load-deflection curves at various parts of tested CMSFs

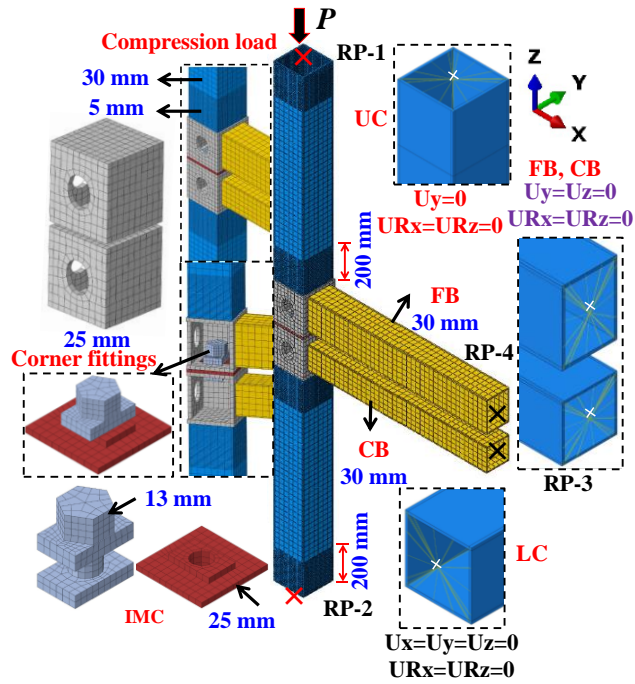
4 Finite element analysis on CMSFs with rotary IMCs

The test yielded valuable data but did not assess CMSF's overall instability and the influence of altering parameters. To create a reliable FEM, test failure modes and data from load-shortening curves were used.

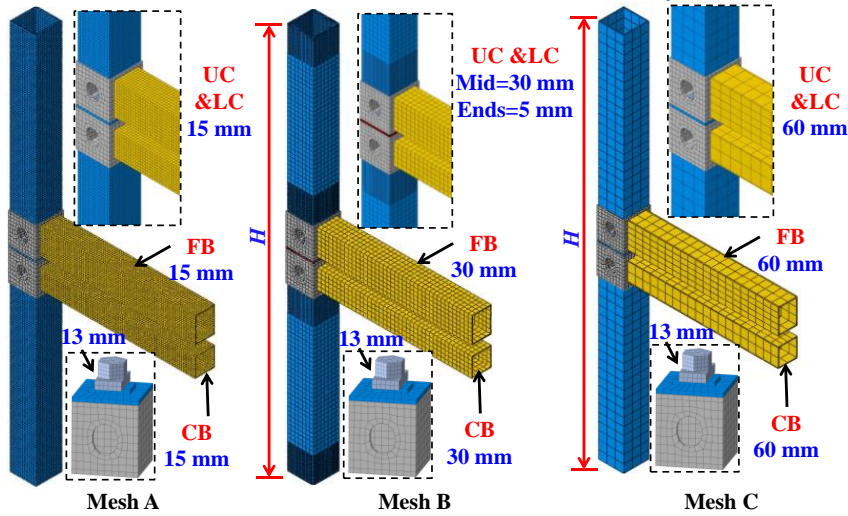
4.1 Formation of finite element model

The finite element modeling and analysis were conducted with ABAQUS [135]. Elastic buckling was performed using the ABAQUS/Linear perturbation buckle-type solver and the subspace iteration approach to determine the buckling loads and modes. Then the nonlinear analysis adopted the ABAQUS/static Riks-type solver to determine the load-shortening and failure mechanism. Moreover, the bilinear kinematic hardening

393 and the von Mises yield criteria were adopted for all components utilizing the associated
 394 material properties listed in **Table 1** [30]. The Poisson's ratio of 0.3 was adopted [78].



395 (a) Verified FEM details of CMSF with rotary IMC



(b) Selected mesh details for FEM validation of CMSF

396
 397 **Fig. 13** Experimentally-verified FEM details of CMSFs with rotary IMCs

398 **4.2 Mesh modeling**

399 **Fig. 13(a)** illustrates the test-validated CMSFs mesh model. Members' dimensions
 400 matched the specimen's design, which was modeled using C3D8R elements [49]. The
 401 suitability of the element size was determined by a mesh convergence study that
 402 employed mesh A, B, and C and compared their results with test $P-\Delta$ curves, as depicted

403 in **Fig. 17(d)**. To accurately replicate local buckling, the column edges at 200 mm were
404 densely meshed, whereas other parts were meshed uniformly. Additionally, the corners
405 of columns and beams were partitioned at their thickness to create the structured mesh
406 [68–71]. Types A and B assessed local buckling and deformation at the column ends
407 more precisely than Type C, shown in supplementary **Fig. B1(h)**. When mesh was
408 raised from 15 to 30 and 60 mm, $P_u (K_e)$ increased by up to 32% (6%) while Δ_u and DI
409 by 11%. Mesh sizes significantly impacted failure modes and compressive behavior,
410 revealing that Type B with 30 mm mesh yielded the closest results. This highlighted
411 the importance of compressive tests on CMSFs with rotary IMCs to determine the
412 proper mesh density.

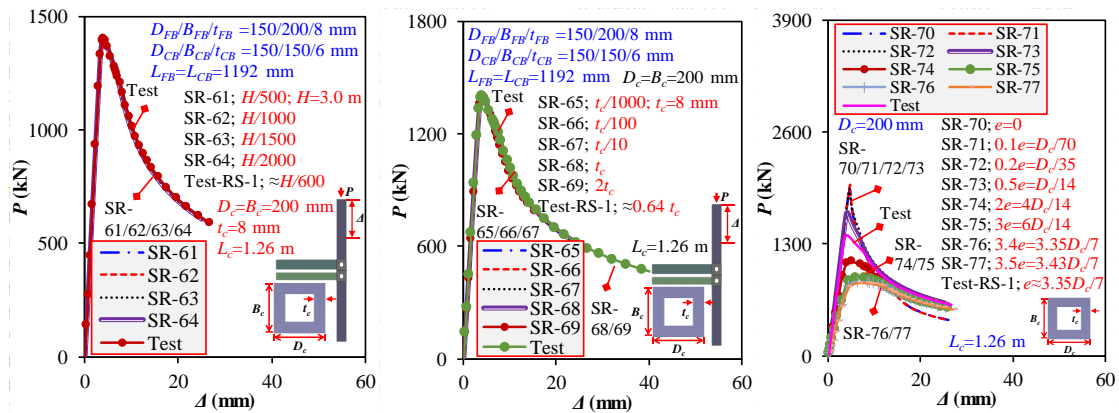
413 **4.3 Loading and boundaries**

414 Reference nodes (RP-1~RP-4) on column and beam cross-sections with surface-based
415 coupling constraints that limit translation and rotation provided loading and boundary
416 conditions. Vertical translations of beams were constrained, whereas those of LCs were
417 restricted in all directions. While UCs and beams had the freedom of in-plane
418 translation, the out-of-plane translation and rotation of beams and columns were
419 restrained. Compression force was applied on the UC as displacement-controlled
420 loading to achieve shortening. Columns and beams were welded to corner fittings using
421 "tie constraint" via surface-to-surface contact. The interaction between corner fittings,
422 connecting plates, and IMC components was simulated as surface-to-surface with "hard
423 contact" as normal while "finite sliding" as tangential behavior [48]. A friction
424 coefficient of 0.3 was chosen, as shown in **Figs. 17(e)** and supplementary **Fig. B1(i)**
425 [49,65]. All specimens used hot-rolled sections with low bending, welding deformation,
426 and residual stresses; thus, the effects of bending, welding, and temperature residual
427 stress were omitted in FEMs [136,137].

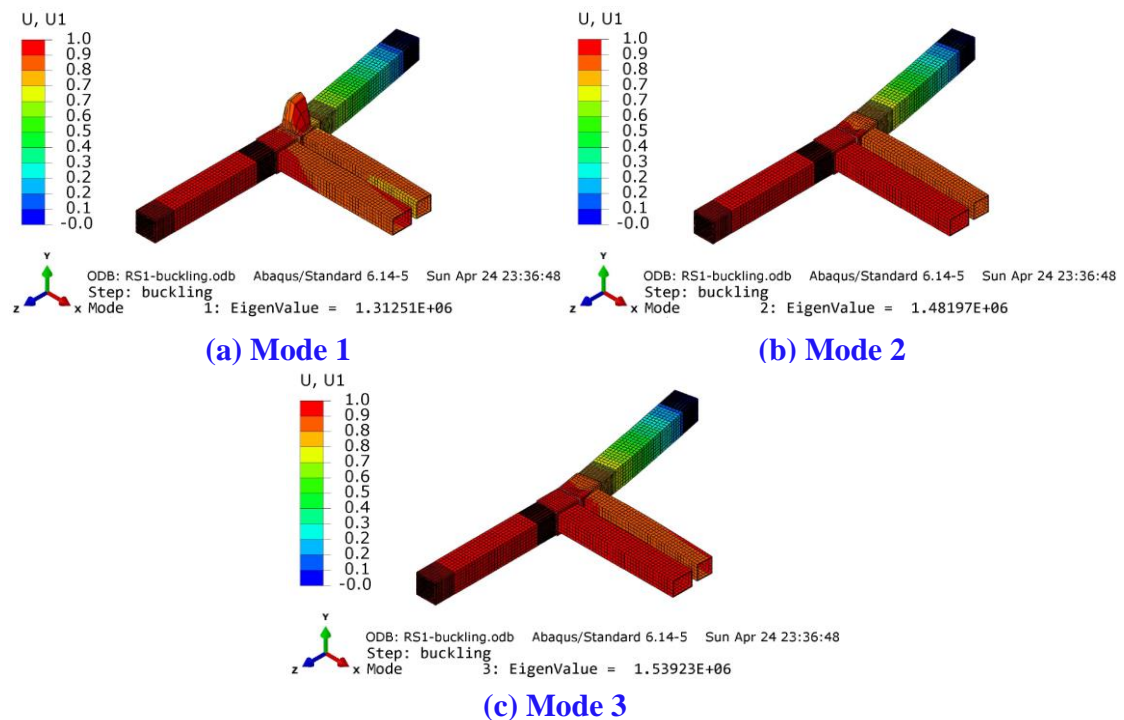
428 **4.4 Initial imperfections**

429 The CMSFs' components might have imperfections before and after installation, which
430 is difficult to measure by conventional methods [134]. Design standards prescribe
431 imperfections between $t_c/500$ to $t_c/200$ and $L_c/1000$ to $L_c/1996$ [138]. However, for
432 CMSFs, imperfections can be attributed to column thickness (t_c), frame height (H), and
433 eccentricity (e) [47,91,92,139]. This study selected height imperfection values of $H/500$,
434 $H/1000$, $H/1500$, and $H/2000$; thickness imperfection values of $t_c/1000$, $t_c/100$, $t_c/10$, t_c ,
435 and $2t_c$; and load eccentricities of 0 , $D_c/70$, $D_c/35$, $D_c/14$, $4D_c/14$, $6D_c/14$, $3.35D_c/7$, and
436 $3.43D_c/7$. Eigenvalue analysis yielded the buckling modes shown in **Fig. 15(a~c)**. In
437 addition to thickness or height imperfections, nonlinear Riks analysis applied load
438 eccentricities per test failure mode depicted in **Fig. 7(a~c)**, such as in the direction of
439 beams for RS1 and RS3 and the opposite direction of beams for RS2. A comparison
440 was made between the critical buckling loads and accompanying mode shapes and the
441 loads at which failure occurred in the Riks analysis. Incorporating global stability
442 parameters offered insights into individual buckling modes' contribution and
443 highlighted local buckling's role in overall stability, improving CMSFs' stability
444 assessment and understanding of buckling modes' interaction. The load corresponding
445 to the first buckling mode was 1312.5 kN for RS1, which exhibited a compressive
446 resistance of 1397 kN. To assure a reliable description of the structure's behavior,
447 imperfections were introduced to the lowest buckling mode (Mode 1) for RS1, RS2,
448 and RS3 [77]. The imperfection amplitude determined in **Fig. 14(a~c)** was utilized for
449 all CMSFs and FEMs in Supplementary **Table A1**. Compared with test results, local
450 imperfection of $H/600$ or $0.64t_c$ and global imperfection of $e=3.35D_c/7$ yielded the
451 closest results. The influence of increasing H or t_c imperfection values on P_u (K_e) and
452 Δ_u (DI) was non-apparent. Since in CMSFs, translation or rotation was allowed; thus

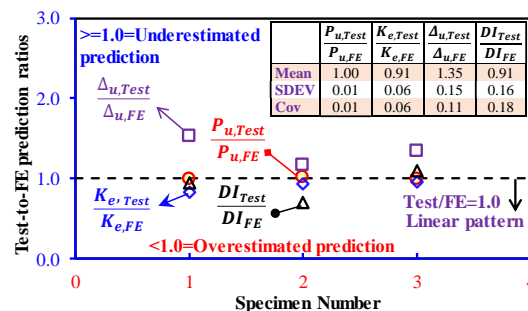
453 the eccentricity impact was significant, as depicted in failure modes in supplementary
 454 **Fig. B1(j).**



455 (a) Local imperfection H (b) Local imperfection t_c (c) Global imperfection e
 456 **Fig. 14** Influence of initial imperfections



457 (a) Mode 1 (b) Mode 2 (c) Mode 3
 458 **Fig. 15** First three buckling modes

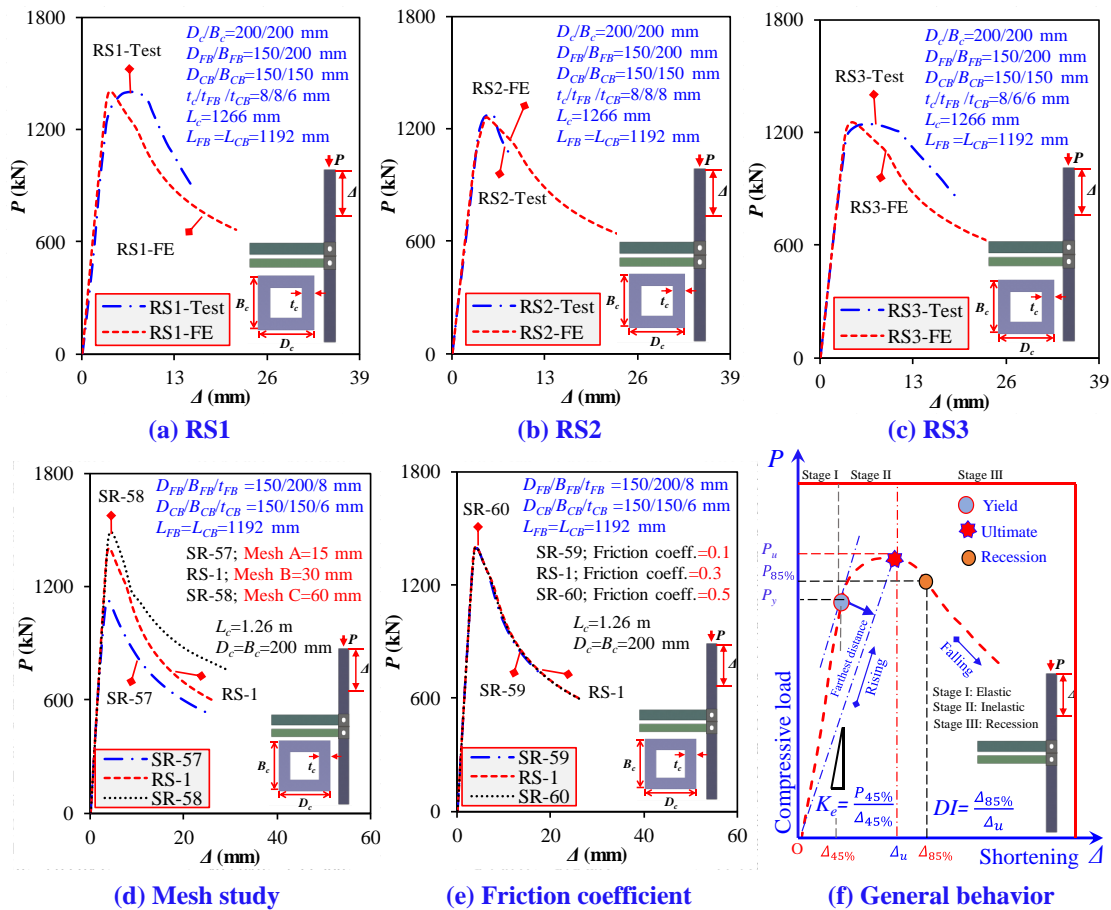


459 **Fig. 16** Comparisons of Tests-to-FEM of CMSFs
 460

461 **4.5 Validations**

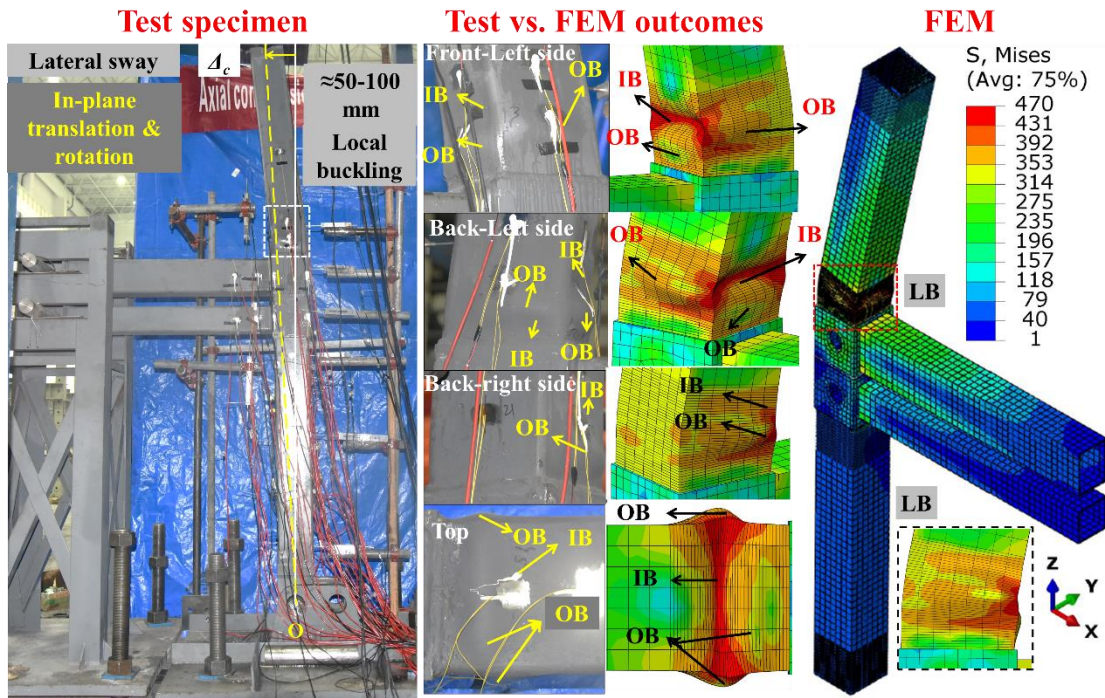
462 The average estimates for P_u , K_e , Δ_u , and DI made by the FEMs for three tests on RS1,
 463 RS2, and RS3 are shown in **Figs. 16 and 17(a~c)**, and **Table 1**. The FEMs produced
 464 average modest prediction errors of 0.3%, 9.1%, and 8.5% for P_u , K_e , and DI but
 465 exhibited a significant scattering of 35% for Δ_u , principally brought on by FEM
 466 simplifications, soft supports, material modeling, and variations in imperfection. The
 467 developed FEM can adequately simulate CMSFs' deformed shapes with inward and
 468 outward LB at the UCs' lower area and sway, as depicted in **Fig. 18(a~c)**, validating
 469 the FEMs' reliability to anticipate the CMSFs' compressive behaviors with rotary IMCs.

470



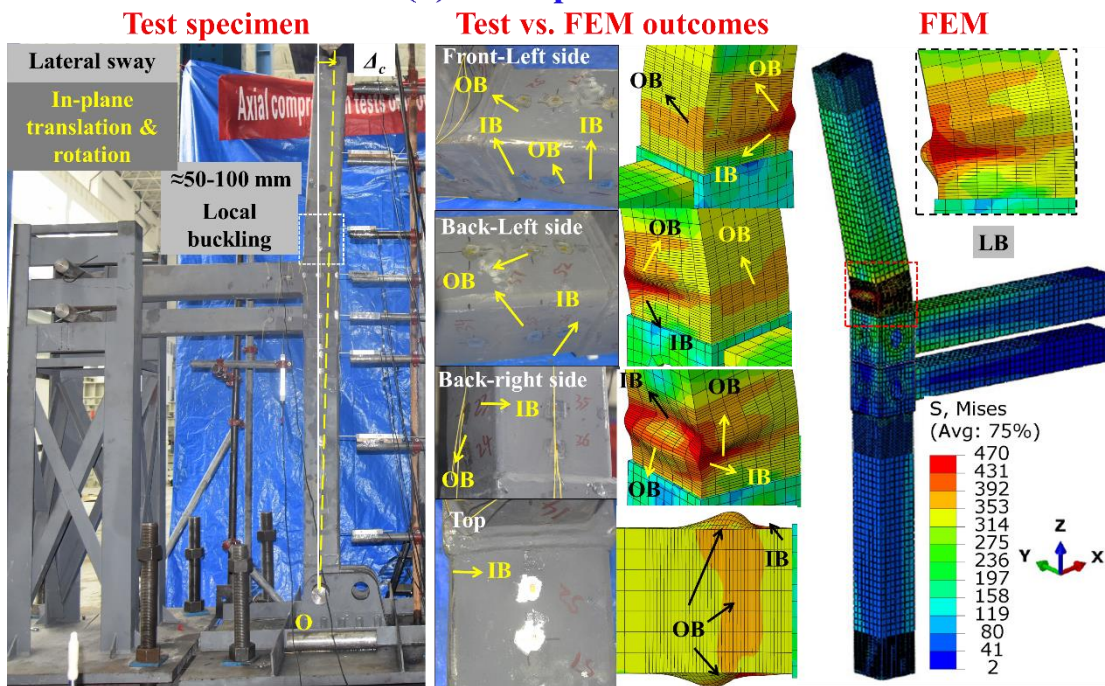
471
472

Fig. 17 Load-shortening curves of CMSFs



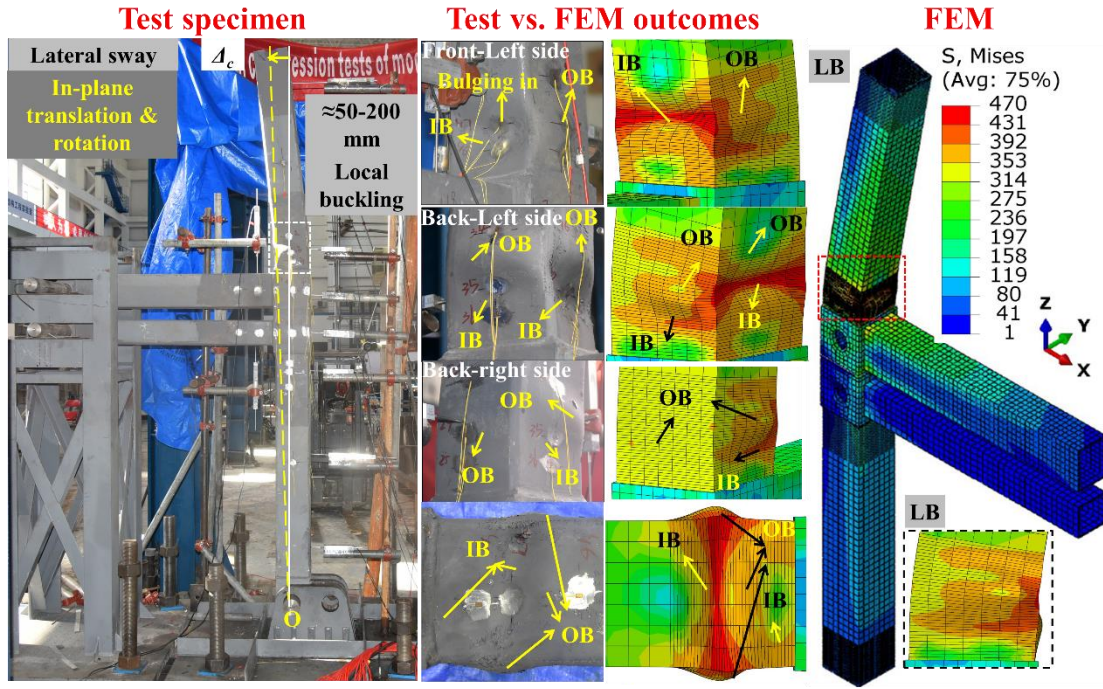
473

(a) RS1 specimen



474

(b) RS2 specimen



(c) RS3 specimen

Fig. 18 Test vs. FE-predicted failure modes

475
476

477 5 Parametric analysis

478 Data for 77 CMSFs was produced using validated FEM that maintained the rotary IMC
 479 and corner fittings dimensions, mesh B, local imperfection of $H/600$ or $0.64t_c$, and
 480 global imperfection of $e=3.35D_c/7$. The parametric analysis covered beam and column
 481 sizes, lengths, spacing, and plate thicknesses. Typical load-shortening and failure
 482 behaviors were classified in Figs. 19(a~g) and 20(a~f), showing similar patterns to the
 483 test results. Supplementary Figs. B1(a~j), B2(a~g), and B3(a~g), along with Table A1,
 484 offered detailed information about the specific parameters and their comprehensive
 485 impact on failure modes, P_u-K_e trends, Δ_u-DI trends, and the values of P_u , K_e , Δ_u , and
 486 DI .

487 5.1 Beams sizes ($D_{FB} \times B_{FB} \times t_{FB}$; $D_{CB} \times B_{CB} \times t_{CB}$)

488 Fig. 19(a) demonstrates how the compressive behavior of CMSFs is influenced by
 489 variations in floor and ceiling beam sizes, such as D_{FB} , D_{CB} , B_{FB} , B_{CB} , t_{FB} , and t_{CB} ,
 490 ranging from 150 to 200 mm and 6 to 8 mm while maintaining their lengths. Increasing
 491 the beam sizes has a positive impact on the CMSFs' performance, enhancing P_u , K_e , Δ_u ,

492 and DI , with improving $P_u (K_e)$ by up to 46% (10%) and $\Delta_u (DI)$ by 15% (19%). This
493 improves frames' compressive behavior and bending resistance. It can prevent
494 premature buckling and improve ductility, allowing CMSFs to deform more before
495 reaching capacity, as shown in Supplementary **Fig. B1(a)**.

496 **5.2 Beams lengths (L_{FB} ; L_{CB})**

497 The compressive behavior of CMSFs can be influenced by floor and ceiling beam
498 length variations, as shown in **Fig. 19(b)**. The results indicate that increasing the beam
499 lengths from 0.6 to 1.2 and 3 m for a given D_{FB} , D_{CB} , B_{FB} , and B_{CB} of 150 and 200 mm
500 and t_{FB} and t_{CB} of 8 and 6 mm could harm the compressive performance of the CMSFs
501 by impairing $P_u (K_e)$ up to 37% (5%). The increased slenderness of longer beams
502 reduces bending resistance and may cause premature buckling, preventing CMSFs from
503 achieving full capacity. Supplementary **Fig. B1(b)** demonstrates that it might improve
504 ductility by enhancing column-beam flexibility when adequately built.

505 **5.3 Columns lengths (L_c)**

506 The compression behavior of CMSFs can be affected by changes in the length of the
507 columns, as depicted in **Fig. 19(c)**. The findings demonstrate that elongating the
508 columns from 0.6 to 1.2 and 3 m for a given L_{FB} and L_{CB} of 0.6, 1.2, and 3 m, D_{FB} , D_{CB} ,
509 B_{FB} , and B_{CB} of 150 and 200 mm, and t_{FB} and t_{CB} of 8 and 6 mm may harm the CMSFs'
510 performance by decreasing their $P_u (K_e)$ by up to 65% (71%). This occurs because
511 longer columns become more slender, reducing their resistance to buckling and bending,
512 which can increase deflection and bending stresses, limiting CMSFs' load-carrying
513 capacity. However, redistribution of forces within the frame might improve the ductility,
514 as demonstrated in Supplementary **Fig. B1(c)**.

515 **5.4 Columns sizes ($D_c \times B_c$)**

516 Changes in the size of the columns can impact the behavior of CMSFs when subjected
517 to compression, as shown in **Fig. 19(d)**. The results indicate that enhancing the cross-

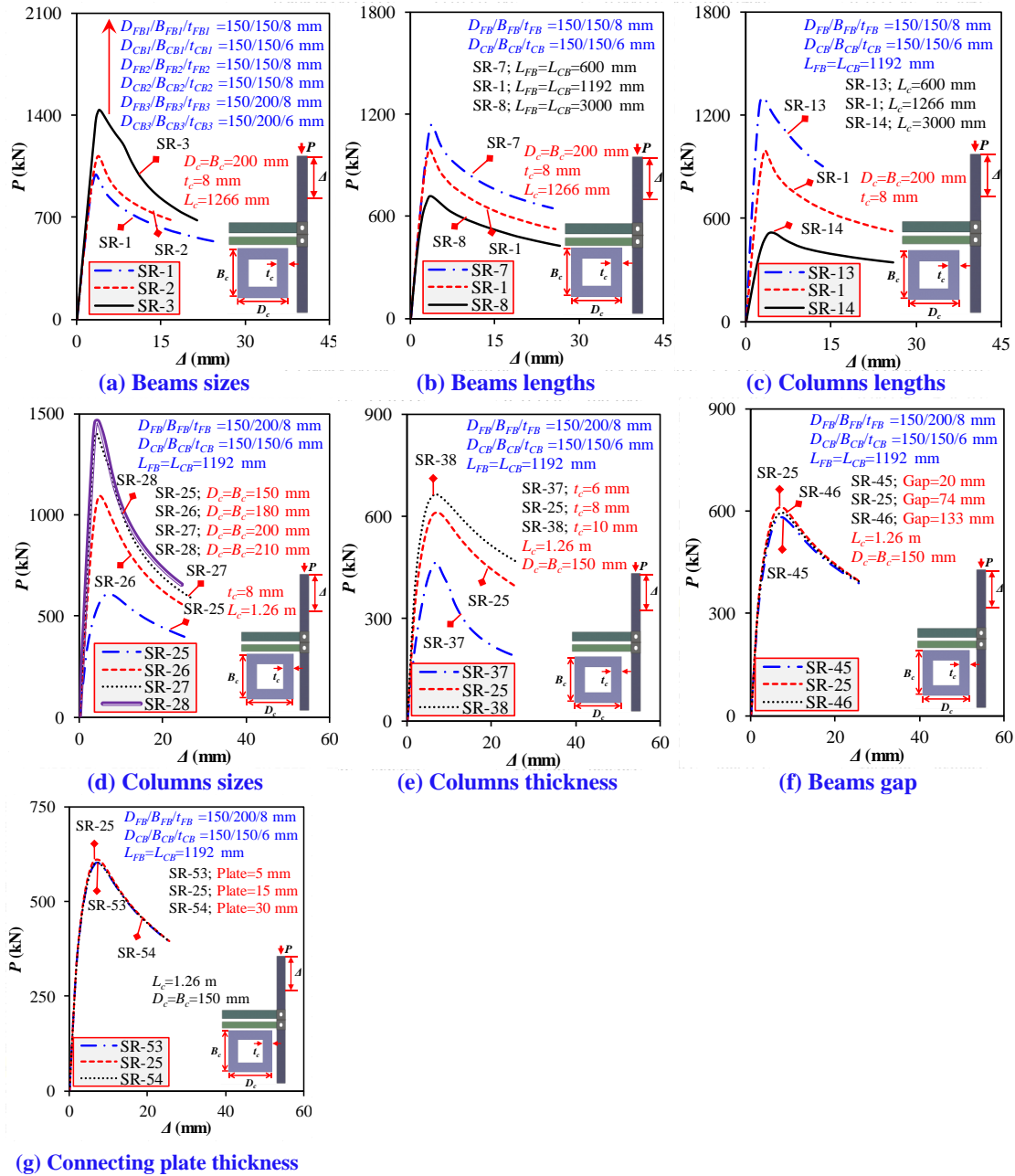
518 sectional sizes from 150 to 180, 200, and 210 mm for a given L_c , L_{FB} , and L_{CB} of 1.2,
519 2.5, and 3.6 m and t_c of 8 mm can improve the performance of CMSFs by increasing
520 their $P_u (K_e)$ up to 140% (116%) but may also have adverse effects by reducing $\Delta_u (DI)$
521 up to 41% (10%). Increasing D_c and B_c improves column buckling and bending
522 resistance and decreases slenderness. As illustrated in Supplementary **Fig. B1(d)**,
523 increasing D_c/t_c yields a wider cross-section, reducing CMSF buckling strain and
524 ductility.

525 **5.5 Columns thickness (t_c)**

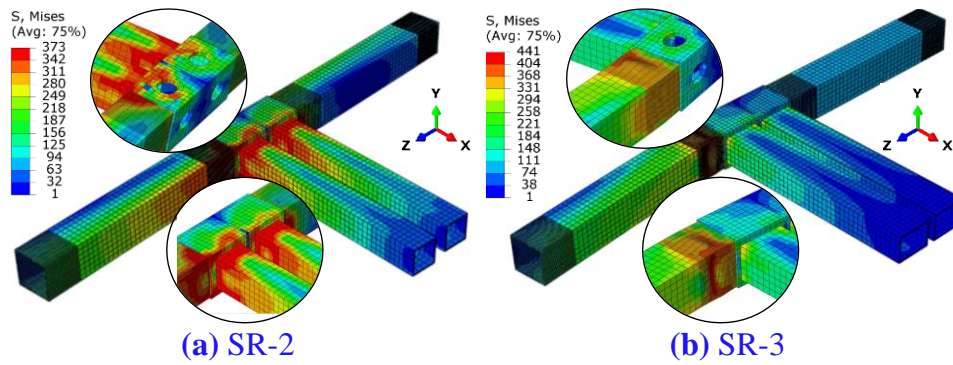
526 In **Fig. 19(e)**, column thickness affects CMSF compression behavior. The results show
527 that increasing column cross-section thickness from 6 to 8 and 10 mm for D_c and B_c of
528 150, 180, 200, and 210 mm can improve CMSF performance by raising their $P_u (K_e)$
529 by up to 123% (55%) and $\Delta_u (DI)$ by up to 16% (113%). A decrease in D_c/t_c reduces
530 column slenderness and increases buckling and bending resistance. Thus, CMSFs can
531 withstand more plastic deformation before failure, increasing their buckling strain and
532 ductility, as depicted in Supplementary **Fig. B1(e)**.

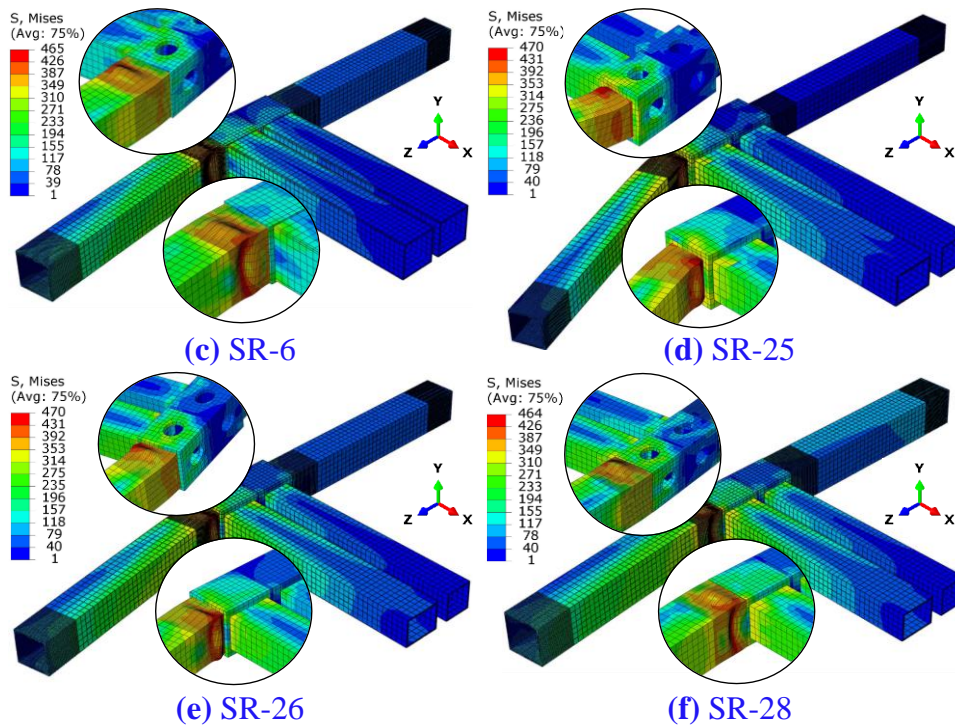
533 **5.6 Beams gap and connecting plate thickness**

534 **Figs. 19(f, g)** and **B1(f, g)** demonstrate that CMSF compressive behavior remained
535 unaffected by increasing the beam gap from 20 to 74 and 133 mm and the connecting
536 plate thickness from 5 to 15 and 30 mm. These factors can affect the frame's lateral
537 rigidity, yet CMSF columns resist compressive stresses, indicating that rotary IMC can
538 transmit compressive loads without localized failure to CMSFs, as depicted in
539 Supplementary **Figs. B1(f)** and **B1(g)** [14,47].



543 **Fig. 19** Influence of varying parameters on CMSFs' load-shortening curves





545

546

547

Fig. 20 CMSFs' typical failure modes against compressive loading

548

6 Theoretical investigations on CMSFs with rotary IMCs

549

The failure mechanism observed in CMSFs reveals both elastic and plastic local inward

550

and outward buckling in the upper columns. This observation indicates noncompliance

551

with EC3 Class 3 slenderness criteria, as elastic buckling is restricted, prohibiting

552

complete cross-section yielding. Local buckling has a significant impact on member

553

capacities, whether it is plastic or elastic [140]. Incorporating global strength while

554

accounting for global stability parameters yields more conservative results than cross-

555

sectional strength assessments under these conditions [86]. Multiple studies

556

demonstrate consistent design practices in which global strength prediction is utilized

557

for member design, considering yield strength failure due to local buckling of Class 3

558

columns [141,142]. Certain investigations include local buckling reduction factors for

559

fixed-ended stubs [143], while others prefer member buckling strength as the primary

560

design criterion [144]. Likewise, global buckling strength models are applied to simple-

561

supported, concentrically compressed members [140]. Notably, IS800 [145,146], NZS

562

3404[147], EC3:1-1 [148], CSA S16-19 [149], AISC360-16 [150], and GB 50017-2017

563 [115] highlight the vitality of effective length factors in stability design, depending on
564 the degree of elastic restraint at frame column ends. The unique characteristics of MSB
565 discontinuous columns and IMCs introduce variability in their effective length factor
566 and buckling load, governed by the relative joint and member bending stiffness ratio
567 and the stiffness of IMCs [81]. Chen et al. [151] underscore that insufficient IMC
568 stiffness can amplify MSB column slenderness, necessitating stability analysis for a
569 conservative determination of critical buckling load. Thus, while assessing CMSF
570 compressive behavior, the critical buckling load that causes the frame to buckle is the
571 main focus. Buckling load equations for the tested sub-assembled CMSFs in **Fig. 21(a)**
572 are determined. The derivation uses pinned and semi-rigid IMCs in three-story full-
573 scale models shown in **Fig. 21(b)**. The stability functions presented in Eqns. 1 and 2
574 [152], along with the buckling load equation in Eqn. 3 [106] are utilized.

$$S_{ii} = \frac{\left(\frac{\pi}{\mu}\right)^2 - \frac{\pi}{\mu} \sin \frac{\pi}{\mu}}{2 - 2 \cos \frac{\pi}{\mu} - \frac{\pi}{\mu} \sin \frac{\pi}{\mu}} ; S_{ij} = \frac{\frac{\pi}{\mu} \sin \frac{\pi}{\mu} - \left(\frac{\pi}{\mu}\right)^2 \cos \frac{\pi}{\mu}}{2 - 2 \cos \frac{\pi}{\mu} - \frac{\pi}{\mu} \sin \frac{\pi}{\mu}} \text{ for } c_1, c_2, \text{ and } c_3 \quad (1)$$

$$S_{ii} = 4 ; S_{ij} = 2 \text{ for } b_1, b_2, b_3, \text{ and } b_4 \quad (2)$$

$$P_{cr} = \left[\frac{\pi^2 EI_{c2}}{(2\mu L_{ct})^2} \right] \quad (3)$$

575 6.1 Pinned IMCs

576 Following Chen et al.'s model [106], using the target column c_2 shown in **Fig. 21(c)**,
577 the members' moments and their equilibrium at joints A, B, and sway are determined
578 from Eqns. 4~8 as follows;

$$(M_A)_{c2} = \left(\frac{EI_{c2}}{L_{c2}} \right) [S_{ii}\theta_A + S_{ij}\theta_B - (S_{ii} + S_{ij}) \Delta_c / L_{ct}] \quad (4)$$

$$(M_B)_{c2} = \left(\frac{EI_{c2}}{L_{c2}} \right) [S_{ij}\theta_A + S_{ii}\theta_B - (S_{ii} + S_{ij}) \Delta_c / L_{ct}] \quad (5)$$

$$(M_A)_{b2} = \left(\frac{EI_{b2}}{L_{b2}} \right) [4\theta_A + 2\theta_B] = \left(\frac{EI_{b2}}{L_{b2}} \right) [6\theta_A] \quad (6)$$

$$(M_B)_{b3} = \left(\frac{EI_{b3}}{L_{b3}} \right) [4\theta_B + 2\theta_A] = \left(\frac{EI_{b3}}{L_{b3}} \right) [6\theta_B] \quad (7)$$

$$(M_A)_{c2} + (M_A)_{b2} = 0; (M_B)_{c2} + (M_B)_{b3} = 0; (M_A)_{c2} + (M_B)_{c2} + P\Delta_c = 0 \quad (8)$$

$$\theta_A(S_{ii} + 6G_C) + \theta_B(S_{ij}) + \Delta_c / L_{ct} [-(S_{ii} + S_{ij})] = 0 ; G_C = \frac{EI_{b2} / L_{b2}}{EI_{c2} / L_{ct}} \quad (9)$$

$$\theta_A(S_{ij}) + \theta_B(S_{ii} + 6G_D) + \Delta_c / L_{ct} [-(S_{ii} + S_{ij})] = 0 ; G_D = \frac{EI_{b3} / L_{b3}}{EI_{c2} / L_{ct}} \quad (10)$$

$$\theta_A(S_{ii} + S_{ij}) + \theta_B(S_{ii} + S_{ij}) - \Delta_c/L_{ct} [2(S_{ii} + S_{ij}) - (\pi^2/\mu^2)] = 0 \quad (11)$$

579 where $P = \frac{\pi^2 EI_{c2}}{\mu^2 L_{c2}^2}$. After solving Eqns. 9~11 using determinant, Eqn. 12 is obtained to

580 calculate the buckling length (μ), which is then inserted in Eqn. 3 to obtain buckling

581 load (P_{cr}/PD) of a sub-assembled CMSF with rotary IMC, assuming as a pinned IMC.

$$\begin{aligned} (S_{ii} + 6G_C) \left[\left\{ \left(\frac{\pi^2}{\mu^2} \right) - 2(S_{ii} + S_{ij}) \right\} \times \{S_{ii} + 6G_D\} + (S_{ii} + S_{ij})^2 \right] \\ - (S_{ij}) \left[\{S_{ij}\} \times \left\{ \left(\frac{\pi^2}{\mu^2} \right) - 2(S_{ii} + S_{ij}) \right\} + (S_{ii} + S_{ij})^2 \right] \\ - (S_{ii} + S_{ij}) \left[(S_{ij}) \times (S_{ii} + S_{ij}) - (S_{ii} + S_{ij}) \times (S_{ii} + 6G_D) \right] = 0 \end{aligned} \quad (12)$$

582 6.2 Semi-rigid IMCs

583 According to Li et al.'s model [99], CMSFs in **Fig. 21(d)** bend in double curvature, so

584 beams' end rotations are equal, such as $\theta_B = \theta_G$; $\theta_C = \theta_H$; $\theta_D = \theta_I$; $\theta_E = \theta_J$. Moreover,

585 column end rotations are $\theta_A = \theta_C - \frac{M_B}{R_{1v}} \times \frac{\theta_D}{\theta_C}$, $\theta_B = \theta_G = \theta_C - \frac{M_B}{R_{1v}}$, $\theta_E = \theta_J = \theta_D - \frac{M_E}{R_{2v}}$, and

586 $\theta_F = \theta_D - \frac{M_E}{R_{2v}} \times \frac{\theta_C}{\theta_D}$. Using slope-deflection equations, the moments of the members are

587 obtained with Eqns. 13~20 as follows;

$$(M_{BA})_{c1} = EI_{c1}/L_{ct} \left[S_{ii} \left(\theta_C - \frac{M_B}{R_{1v}} \right) + S_{ij} \left(\theta_D - \frac{M_B}{R_{1v}} \times \frac{\theta_D}{\theta_C} \right) - (S_{ii} + S_{ij}) \Delta_c/L_{ct} \right] \quad (13)$$

$$(M_{CD})_{c2} = EI_{c2}/L_{ct} \left[S_{ii} \theta_C + S_{ij} \theta_D - (S_{ii} + S_{ij}) \Delta_c/L_{ct} \right] \quad (14)$$

$$(M_{DC})_{c2} = EI_{c2}/L_{ct} \left[S_{ii} \theta_D + S_{ij} \theta_C - (S_{ii} + S_{ij}) \Delta_c/L_{ct} \right] \quad (15)$$

$$(M_{EF})_{c3} = EI_{c3}/L_{ct} \left[S_{ii} \left(\theta_D - \frac{M_E}{R_{2v}} \right) + S_{ij} \left(\theta_C - \frac{M_E}{R_{2v}} \times \frac{\theta_C}{\theta_D} \right) - (S_{ii} + S_{ij}) \Delta_c/L_{ct} \right] \quad (16)$$

$$(M_{BG})_{b1} = 6 \left(EI_{b1}/L_{b1} \right) \theta_B = 6 \left(EI_{b1}/L_{b1} \right) \left(\theta_C - \frac{M_B}{R_{1v}} \right) \quad (17)$$

$$(M_{CH})_{b2} = 6 \left(EI_{b2}/L_{b2} \right) \theta_C \quad (18)$$

$$(M_{DI})_{b3} = 6 \left(EI_{b3}/L_{b3} \right) \theta_D \quad (19)$$

$$(M_{EJ})_{b4} = 6 \left(EI_{b4}/L_{b4} \right) \theta_E = 6 \left(EI_{b4}/L_{b4} \right) \left(\theta_D - \frac{M_E}{R_{2v}} \right) \quad (20)$$

588 Using c_2 as the objective column, the equilibrium of moments at joints C, D, and sway

589 can be calculated using Eqns. 21~23.

$$(M_{BA})_{c1} + (M_{BG})_{b1} + (M_{CH})_{b2} + (M_{CD})_{c2} = 0 \quad (21)$$

$$(M_{EF})_{c3} + (M_{EJ})_{b4} + (M_{DI})_{b3} + (M_{DC})_{c2} = 0 \quad (22)$$

$$(M_{CD})_{c2} + (M_{DC})_{c2} + P \Delta_c = 0 \quad (23)$$

590 Eqn. 23 is used to determine $\Delta_c/L_{ct} = \frac{\mu^2(S_{ii}+S_{ij})(\theta_c+\theta_D)}{-\pi^2+2(S_{ii}+S_{ij})\mu^2}$ by substituting $P = \frac{\pi^2 EI_{c2}}{\mu^2 L_{c2}^2}$. By
591 introducing Δ_c/L_{ct} , Eqns. 13~20, relative beam-column stiffness ratios, i.e., $G_{1v} =$
592 $\frac{EI_{b1}/L_{b1}}{EI_{c1}/L_{ct}}$, $G_{2v} = \frac{EI_{b2}/L_{b2}}{EI_{c2}/L_{ct}}$, $G_{3v} = \frac{EI_{b3}/L_{b3}}{EI_{c2}/L_{ct}}$, and $G_{4v} = \frac{EI_{b4}/L_{b4}}{EI_{c3}/L_{ct}}$, and IMC-to-column stiffness ratios,
593 i.e., $J_{1v} = \frac{R_{1v}}{EI_{c1}/L_{ct}}$, $J_{2v} = \frac{R_{1v}}{EI_{c2}/L_{ct}}$, $J_{3v} = \frac{R_{2v}}{EI_{c2}/L_{ct}}$, and $J_{4v} = \frac{R_{2v}}{EI_{c3}/L_{ct}}$ into Eqns. 21 and 22, Eqns.
594 24 and 25 can be rearranged in the form of θ_c^2 , θ_D^2 , and $\theta_c\theta_D$.

$$\begin{aligned} & \theta_c^2 \left[(6G_{1v} + S_{ii})(6G_{2v} + S_{ii}) + (6G_{1v}J_{2v} + 6G_{2v}J_{1v} + S_{ii}J_{2v} + S_{ii}J_{1v}) - \right. \\ & \quad \left. \frac{\mu^2}{-\pi^2+2(S_{ii}+S_{ij})\mu^2} (6G_{1v} + S_{ii} + J_{1v} + J_{2v})(S_{ii} + S_{ij})^2 \right] + \theta_D^2 \left[S_{ij}^2 - \right. \\ & \quad \left. \frac{\mu^2}{-\pi^2+2(S_{ii}+S_{ij})\mu^2} S_{ij}(S_{ii} + S_{ij})^2 \right] + \theta_c\theta_D \left[S_{ij}(J_{2v} + J_{1v} + 6G_{2v} + 2S_{ii} + 6G_{1v}) - \right. \\ & \quad \left. \frac{\mu^2}{-\pi^2+2(S_{ii}+S_{ij})\mu^2} (6G_{1v} + S_{ii} + J_{1v} + J_{2v})(S_{ii} + S_{ij})^2 - \frac{\mu^2}{-\pi^2+2(S_{ii}+S_{ij})\mu^2} S_{ij}(S_{ii} + \right. \\ & \quad \left. S_{ij})^2 \right] = 0 \end{aligned} \quad (24)$$

$$\begin{aligned} & \theta_D^2 \left[(6G_{3v} + S_{ii})(6G_{4v} + S_{ii}) + (6G_{4v}J_{3v} + 6G_{3v}J_{4v} + S_{ii}J_{4v} + S_{ii}J_{3v}) - \right. \\ & \quad \left. \frac{\mu^2}{-\pi^2+2(S_{ii}+S_{ij})\mu^2} (6G_{4v} + S_{ii} + J_{4v} + J_{3v})(S_{ii} + S_{ij})^2 \right] + \theta_c^2 \left[S_{ij}^2 - \right. \\ & \quad \left. \frac{\mu^2}{-\pi^2+2(S_{ii}+S_{ij})\mu^2} S_{ij}(S_{ii} + S_{ij})^2 \right] + \theta_c\theta_D \left[S_{ij}(J_{3v} + J_{4v} + 6G_{3v} + 2S_{ii} + 6G_{4v}) - \right. \\ & \quad \left. \frac{\mu^2}{-\pi^2+2(S_{ii}+S_{ij})\mu^2} (6G_{4v} + S_{ii} + J_{4v} + J_{3v})(S_{ii} + S_{ij})^2 - \frac{\mu^2}{-\pi^2+2(S_{ii}+S_{ij})\mu^2} S_{ij}(S_{ii} + \right. \\ & \quad \left. S_{ij})^2 \right] = 0 \end{aligned} \quad (25)$$

$$(\theta_c + \beta_1\theta_D)(\beta_2\theta_c + \beta_3\theta_D) = 0; (\beta_4\theta_c + \theta_D)(\beta_5\theta_c + \beta_6\theta_D) = 0 \quad (26)$$

595 Eqn. 26 is a simplified representation of Eqns. 24 and 25, having four general solutions,
596 i.e., $\begin{vmatrix} 1 & \beta_1 \\ \beta_4 & 1 \end{vmatrix} = 0$; $\begin{vmatrix} 1 & \beta_1 \\ \beta_5 & \beta_6 \end{vmatrix} = 0$; $\begin{vmatrix} \beta_2 & \beta_3 \\ \beta_4 & 1 \end{vmatrix} = 0$; $\begin{vmatrix} \beta_2 & \beta_3 \\ \beta_5 & \beta_6 \end{vmatrix} = 0$. Eqns. 27~30 provide simplified
597 expressions resulting from solving these general solutions' determinants. The minimum
598 buckling load (P_{cr}/SR) of a sub-assembled CMSF with a rotary IMC, assuming as a
599 semi-rigid IMC, can be obtained by inserting the buckling length (μ) calculated from
600 the maximum value obtained from Eqns. 27~30 into Eqn. 3.

$$601 \quad 1 - \left[\frac{2[S_{ij}^2-D]}{[S_{ij}(E)-C-D]+\sqrt{[S_{ij}(E)-C-D]^2-4[S_{ij}^2-D][A+B-C]}} \right] \left[\frac{2[S_{ij}^2-I]}{[S_{ij}J-H-I]+\sqrt{[S_{ij}J-H-I]^2-4[F+G-H][S_{ij}^2-I]}} \right] = 0 \quad (27)$$

$$602 \quad [F + G - H] - \left[\frac{2[S_{ij}^2 - D]}{[S_{ij}(E) - C - D] + \sqrt{[S_{ij}(E) - C - D]^2 - 4[S_{ij}^2 - D][A + B - C]}} \right] \left[\frac{[S_{ij}J - H - I] + \sqrt{[S_{ij}J - H - I]^2 - 4[F + G - H][S_{ij}^2 - I]}}{2} \right] =$$

$$603 \quad 0 \quad (28)$$

$$604 \quad [A + B - C] - \left[\frac{[S_{ij}(E) - C - D] + \sqrt{[S_{ij}(E) - C - D]^2 - 4[S_{ij}^2 - D][A + B - C]}}{2} \right] \left[\frac{2[S_{ij}^2 - I]}{[S_{ij}J - H - I] + \sqrt{[S_{ij}J - H - I]^2 - 4[F + G - H][S_{ij}^2 - I]}} \right] =$$

$$605 \quad 0 \quad (29)$$

$$606 \quad [A + B - C][F + G - H] -$$

$$607 \quad \left[\frac{[S_{ij}(E) - C - D] + \sqrt{[S_{ij}(E) - C - D]^2 - 4[S_{ij}^2 - D][A + B - C]}}{2} \right] \left[\frac{[S_{ij}J - H - I] + \sqrt{[S_{ij}J - H - I]^2 - 4[F + G - H][S_{ij}^2 - I]}}{2} \right] = 0 \quad (30)$$

608 Coefficients A , B , C , D , E , F , G , and H in Eqns. 27~30 are derived from Eqns. 31~34,
609 which are defined in Eqns. 24 and 25 for θ_C^2 , θ_D^2 , and $\theta_C\theta_D$. The rotational
610 stiffnesses of rotary IMCs are $R_{1v} = R_{2v} = 2391.49$ kNm/rad, as reported in [26].

$$A = (6G_{1v} + S_{ii})(6G_{2v} + S_{ii}); B = (6G_{1v}J_{2v} + 6G_{2v}J_{1v} + S_{ii}J_{2v} + S_{ii}J_{1v}) \quad (31)$$

$$C = \frac{\mu^2(6G_{1v} + S_{ii} + J_{1v} + J_{2v})(S_{ii} + S_{ij})^2}{-\pi^2 + 2(S_{ii} + S_{ij})\mu^2}; D = \frac{\mu^2 S_{ij}(S_{ii} + S_{ij})^2}{-\pi^2 + 2(S_{ii} + S_{ij})\mu^2} \quad (32)$$

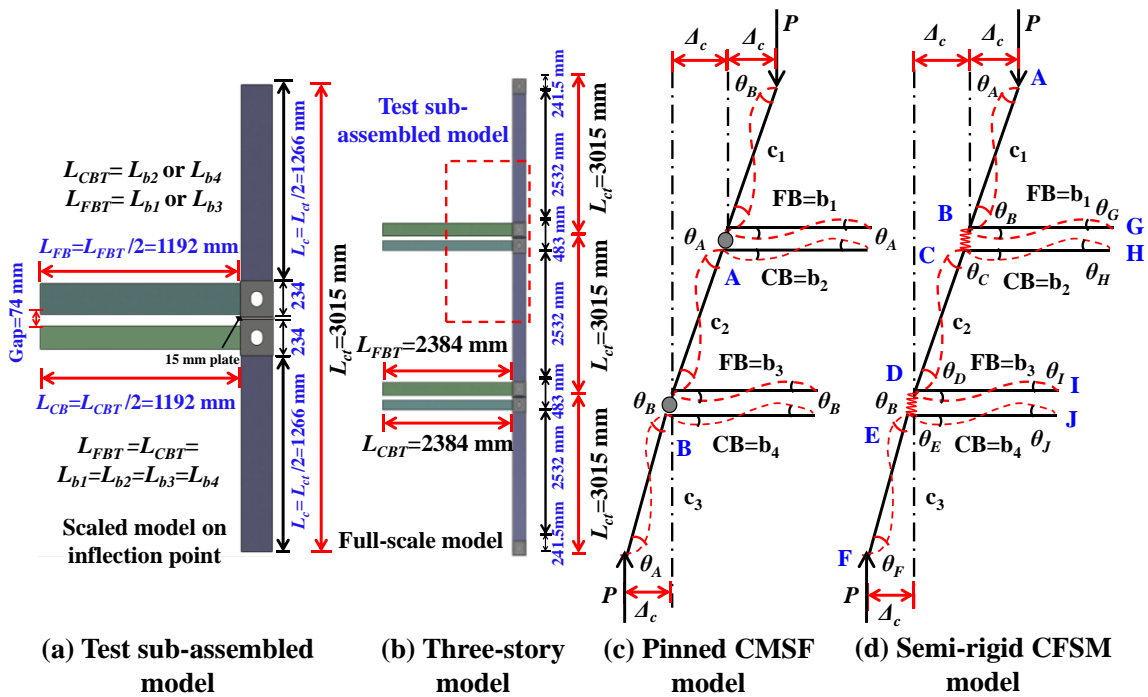
$$E = (J_{2v} + J_{1v} + 6G_{2v} + 2S_{ii} + 6G_{1v}); F = (6G_{3v} + S_{ii})(6G_{4v} + S_{ii}) \quad (33)$$

$$G = (6G_{4v}J_{3v} + 6G_{3v}J_{4v} + S_{ii}J_{4v} + S_{ii}J_{3v}); H = \frac{\mu^2(6G_{4v} + S_{ii} + J_{4v} + J_{3v})(S_{ii} + S_{ij})^2}{-\pi^2 + 2(S_{ii} + S_{ij})\mu^2} \quad (34)$$

611 6.3 Validations

612 **Fig. 22** and **Table 2** compare FEMs' buckling loads (P_{cr}/FE) to theoretical ones
613 (P_{cr}/PD and P_{cr}/SR). The average (Covs) prediction ratios with P_{cr}/PD and P_{cr}/SR
614 are 0.70(0.17) and 0.96(0.09), offering averagely conservative results. However,
615 P_{cr}/PD underestimates findings across a wider range, but P_{cr}/SR minimizes
616 dispersion and produces more accurate results. Despite this, it is still important to
617 account for safety factors due to minor overestimates caused by uncertainties associated
618 with inflection points, semi-rigid behavior, and rotational stiffness. Results indicate that
619 the buckling load prediction of sub-assembled CMSFs could be accurately anticipated
620 by considering rotary IMC's rotational stiffness of $R_{1v} = R_{2v} = 2391.49$ kNm/rad [26].
621 Alternately, presuming rotary IMC as pinned could not reflect CMSFs' actual
622 compressive behavior and could lead to an uneconomical design. Using pinned
623 assumptions to estimate the buckling load yields conservative values that do not

624 account for IMCs and apply to all CMSFs. However, sub-assembled CMSF forecasts
 625 are more accurate when IMCs are considered semi-rigid. In worst-case scenarios, these
 626 equations' conservative nature can impact CMSF design standards. When the other
 627 forces acting are small, or the frame has significant rigidity against deformations, these
 628 equations can be used to design the dimensions of the members and predict the buckling
 629 lengths and loads for CMSF, considering the stiffnesses of its members and IMCs under
 630 axial compressions. However, the findings are limited to specific models and require
 631 further validation. The outcomes do not apply to non-sway or special frames with
 632 welded IMCs or shear-keyed columns. The study's exterior-frame findings can be used
 633 to design middle or inner CMSFs by modifying the number of frames.



634 (a) Test sub-assembled model (b) Three-story model (c) Pinned CMSF model (d) Semi-rigid CFSM model
 635 **Fig. 21** Theoretical buckling load sub-assembled models; Chen et al.'s model [106]
 636 for pinned and Li et al.'s model [99] for semi-rigid CMSFs

637
638

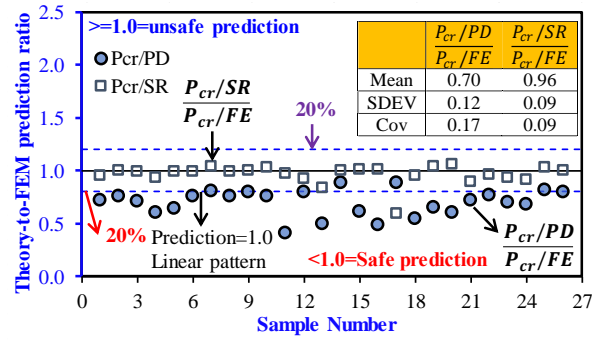


Fig. 22 Comparison of Theory-to-FEM

Table 2 Comparison of CMSFs' buckling load via tests-validated FEMs, parametric studies, and theoretical models

Test specimen (#)	P_{cr}/FE (kN)	P_{cr}/PD (kN)	P_{cr}/SR (kN)	$\frac{P_{cr}/PD}{P_{cr}/FE}$	$\frac{P_{cr}/SR}{P_{cr}/FE}$
RS1	1312.5	939.4	1248.3	0.72	0.95
RS2	1342.4	1019.4	1336.6	0.76	1.00
RS3	1241.3	885.6	1234.4	0.71	0.99
Mean				0.73	0.98
Cov				0.03	0.02
FEM (#)	P_{cr}/FE (kN)	P_{cr}/PD (kN)	P_{cr}/SR (kN)	$\frac{P_{cr}/PD}{P_{cr}/FE}$	$\frac{P_{cr}/SR}{P_{cr}/FE}$
SR-1	1304.2	783.6	1210.4	0.60	0.93
SR-2	1321.4	849.9	1302.9	0.64	0.99
SR-3	1514.2	1155.2	1496.1	0.76	0.99
SR-4	1522.0	1228.2	1587.5	0.81	1.04
SR-5	1670.5	1272.4	1659.8	0.76	0.99
SR-6	1670.0	1343.3	1665.1	0.80	1.00
SR-7	1529.9	1157.5	1579.4	0.76	1.03
SR-8	958.9	390.6	932.3	0.41	0.97
SR-9	1888.8	1506.3	1742.0	0.80	0.92
SR-10	1322.0	664.5	1111.9	0.50	0.84
SR-11	1796.5	1599.1	1802.8	0.89	1.00
SR-12	1269.2	770.9	1281.5	0.61	1.01
SR-13	3337.8	1650.7	3386.2	0.49	1.01
SR-26	1353.1	1203.5	801.0	0.89	0.59
SR-28	1829.2	1002.9	1743.4	0.55	0.95
SR-40	1349.1	880.5	1397.5	0.65	1.04
SR-42	1701.8	1019.6	1796.1	0.60	1.06
SR-47	1110.8	801.0	1003.0	0.72	0.90
SR-48	1042.1	801.0	1003.0	0.77	0.96
SR-49	1336.7	939.4	1248.3	0.70	0.93
SR-50	1373.3	939.4	1248.3	0.68	0.91
SR-51	1330.3	1093.8	1376.1	0.82	1.03
SR-52	1372.4	1093.8	1376.1	0.80	1.00
Mean				0.70	0.96
Cov				0.18	0.10

P_{cr}/FE , P_{cr}/PD , and P_{cr}/SR define the buckling load of sub-assembled CMSFs with rotary IMC obtained through experimentally-validated FEMs and theoretical models with pinned and semi-rigid IMCs. FE represents the FEM, PD denotes the pinned IMC model, and SR defines the semi-rigid IMC model.

639 **7 Conclusions**

640 This study comprehensively investigated the compressive behaviors of CMSFs with
641 rotary IMC through sub-assembled tests, parametric FEMs, and theoretical buckling
642 load models. The research yielded the following key findings:

- 643 1. The load-shortening behaviors of CMSFs displayed elastic, inelastic, and
644 recessional characteristics. Local buckling occurred on the upper columns
645 initiated from the bending sides to the adjacent faces, resulting in a reduction in
646 capacity, amplified buckling, and apparent sway of the CMSFs.
- 647 2. All CMSFs experienced the same failure mode, but the beams' rigidity
648 influenced the direction of sway. Frames and columns tended to sway towards
649 the beams when thinner while bending occurred in the opposite direction when
650 beams were more rigid.
- 651 3. The strain curves revealed that only the upper columns had local buckling, either
652 inward or outward, occurring similarly on opposite sides and oppositely on
653 neighboring sides. Elastic buckling developed on columns opposite the bending
654 direction, while plastic buckling occurred on adjacent sides. No failure,
655 buckling, or yielding was noticed in other members and IMCs.
- 656 4. Increasing the cross-sectional sizes of beams and columns improved the
657 compressive resistance and rigidity of CMSFs while lengthening members
658 impaired them. Greater member rigidity reduced buckling strain and ductility,
659 causing premature instability.
- 660 5. The FEM with a mesh of 30 mm, local imperfection of $H/600$ or $0.64t_c$, and
661 global imperfection of $e=3.35D_c/7$ accurately simulated CMSFs' compression
662 behavior with average prediction errors of 0.3% for P_u .

663 6. The mean (Cov) theory-to-FEM buckling load for pinned and semi-rigid
664 CMSFs was 0.70(0.17) and 0.96(0.09), indicating that the semi-rigid model
665 provided more precise outcomes with reduced scatter and can accurately predict
666 CMSFs' compressive behavior with rotary IMC.

667 **8 Design recommendations and future research**

668 The extensive research into the compressive behavior of CMSFs with rotary IMCs
669 holds substantial significance for the structural integrity and stability of MSBs,
670 providing valuable insights into modular frame failure modes and capacity. As the
671 results indicate, incorporating rotary IMCs into structural designs necessitates
672 considering the rotational stiffness and behavioral characteristics [17,26]. Meeting
673 performance requirements demand structural members with an appropriate size and
674 stiffness. Parametric studies show that increasing column and beam cross-sectional
675 sizes and thicknesses improves strength; hence, using IMCs with superior geometrical
676 designs could enhance capacity. Moreover, FEMs and theoretical calculations have
677 been verified with experimental and numerical data to estimate buckling loads and
678 failure mechanisms accurately. The complexity and unexpected behavior of IMCs
679 makes designing and analyzing with pinned and rigid assumptions difficult. However,
680 the theoretical models presented in this study provide a systematic classification scheme
681 for pinned and semi-rigid IMCs, enabling interconnection behavior prediction and
682 modular system reliability improvement. Effectively regulating relative stiffnesses
683 based on these models can result in conservative and cost-effective design choices.

684 Future studies could examine different IMC types' performance to understand their
685 distinct characteristics, potential advantages in multiple applications, and applicability
686 of design models. Using grouped columns, beams, and horizontal and vertical IMCs,
687 middle and interior CMSFs can be studied in modular frame systems. Simplified FEMs

688 using rotary IMCs spring models could help design multi-story building systems more
689 precisely and efficiently. Such study is essential to MSB development and practical
690 efficacy and safety.

691 **Acknowledgment**

692 The authors acknowledge the National Natural Science Foundation of China for
693 financially supporting their research (Grant No. 51978457 and 52008292). The
694 authors are appreciative of the invaluable suggestions and time spent by the editors
695 and reviewers in enhancing the quality of the paper.

696 **References**

- 697 [1] Jaillon L, Poon CS. The evolution of prefabricated residential building systems in Hong Kong:
698 A review of the public and the private sector. *Autom Constr* 2009;18:239–48.
699 <https://doi.org/10.1016/j.autcon.2008.09.002>.
- 700 [2] Liu Y, Chen Z, Liu J, Bai Y, Zhong X, Wang X. Lateral stiffness evaluation on corner-supported
701 thin walled modular steel structures. *Thin-Walled Struct* 2020;157:106967.
702 <https://doi.org/10.1016/j.tws.2020.106967>.
- 703 [3] Chen LK, Yuan RP, Ji XJ, Lu XY, Xiao J, Tao JB, et al. Modular composite building in urgent
704 emergency engineering projects: A case study of accelerated design and construction of Wuhan
705 Thunder God Mountain/Leishenshan hospital to COVID-19 pandemic. *Autom Constr*
706 2021;124:103555. <https://doi.org/10.1016/j.autcon.2021.103555>.
- 707 [4] Chen Z, Khan K, Khan A, Javed K, Liu J. Exploration of the multidirectional stability and
708 response of prefabricated volumetric modular steel structures. *J Constr Steel Res*
709 2021;184:106826. <https://doi.org/10.1016/j.jcsr.2021.106826>.
- 710 [5] Corfar D, Tsavdaridis KD. A comprehensive review and classification of inter-module
711 connections for hot-rolled steel modular building systems. *J Build Eng* 2022;50:104006.
712 <https://doi.org/10.1016/j.jobe.2022.104006>.
- 713 [6] Ferdous W, Bai Y, Duc T, Manalo A, Mendis P. New advancements , challenges and
714 opportunities of multi-storey modular buildings – A state-of-the-art review. *Eng Struct*
715 2019;183:883–93. <https://doi.org/10.1016/j.engstruct.2019.01.061>.
- 716 [7] Srisangeerthan S, Hashemi MJ, Rajeev P, Gad E, Fernando S. Review of performance
717 requirements for inter-module connections in multi-story modular buildings. *J Build Eng*
718 2020;28:101087. <https://doi.org/10.1016/j.jobe.2019.101087>.
- 719 [8] Ye Z, Giriunas K, Sezen H, Wu G, Feng D. State-of-the-art review and investigation of structural
720 stability in multi-story modular buildings. *J Build Eng* 2021;33:101844.
721 <https://doi.org/10.1016/j.jobe.2020.101844>.
- 722 [9] Deng E, Zong L, Ding Y, Zhang Z, Zhang J, Shi F. Seismic performance of mid-to-high rise
723 modular steel construction - A critical review. *Thin-Walled Struct* 2020;155:106924.
724 <https://doi.org/10.1016/j.tws.2020.106924>.
- 725 [10] Thai H, Ngo T, Uy B. A review on modular construction for high-rise buildings. *Structures*
726 2020;28:1265–90. <https://doi.org/10.1016/j.istruc.2020.09.070>.
- 727 [11] Lacey AW, Chen W, Hao H, Bi K. Structural response of modular buildings – An overview. *J*
728 *Build Eng* 2018;16:45–56. <https://doi.org/10.1016/j.jobe.2017.12.008>.
- 729 [12] Lawson RM, Ogden RG. “Hybrid” light steel panel and modular systems. *Thin-Walled Struct*
730 2008;46:720–30. <https://doi.org/10.1016/j.tws.2008.01.042>.

- 731 [13] Mark Lawson, Ray Odgen CG. Design in Modular Construction Design in Construction. CRC
732 Press Web; 2014.
- 733 [14] Lacey AW, Chen W, Hao H. Experimental methods for inter-module joints in modular building
734 structures – A state-of-the-art review. *J Build Eng* 2022;46:103792.
735 <https://doi.org/10.1016/j.jobe.2021.103792>.
- 736 [15] Shi F, Ding Y, Zong L, Meng X, Chen Y. Axial mechanical behavior of innovative inter-module
737 connection for modular steel constructions. *J Build Eng* 2023;65:105765.
738 <https://doi.org/10.1016/j.jobe.2022.105765>.
- 739 [16] Dai X, Zong L, Ding Y, Li Z. Experimental study on seismic behavior of a novel plug-in self-
740 lock joint for modular steel construction. *Eng Struct* 2019;181:143–64.
741 <https://doi.org/10.1016/j.engstruct.2018.11.075>.
- 742 [17] Chen Z, Wang J, Liu J, Cong Z. Tensile and shear performance of rotary inter-module connection
743 for modular steel buildings. *J Constr Steel Res* 2020;175:106367.
744 <https://doi.org/10.1016/j.jcsr.2020.106367>.
- 745 [18] Yang N, Xia J, Chang H, Zhang L, Yang H. A novel plug-in self-locking inter-module connection
746 for modular steel buildings. *Thin-Walled Struct* 2023;187:110774.
747 <https://doi.org/10.1016/j.tws.2023.110774>.
- 748 [19] Lacey AW, Chen W, Hao H, Bi K, Tallowin FJ. Shear behaviour of post-tensioned inter-module
749 connection for modular steel buildings. *J Constr Steel Res* 2019;162:105707.
750 <https://doi.org/10.1016/j.jcsr.2019.105707>.
- 751 [20] Lacey AW, Chen W, Hao H, Bi K. New interlocking inter-module connection for modular steel
752 buildings: Experimental and numerical studies. *Eng Struct* 2019;198:109465.
753 <https://doi.org/10.1016/j.engstruct.2019.109465>.
- 754 [21] Doh J, Ho NM, Miller D, Peters T, Carlson D, La P. Steel Bracket Connection on Modular
755 Buildings. *J Steel Struct Constr* 2016. <https://doi.org/10.4172/2472-0437.1000121>.
- 756 [22] Shi F, Ding Y, Zong L, Chen Y, Wu Y. Shear behaviour of vertical inter-module connection with
757 bolts and shear keys for MSCs. *Structures* 2023;47:260–81.
758 <https://doi.org/10.1016/j.istruc.2022.11.046>.
- 759 [23] Nadeem G, Azizi N, Abu N, Abd I. Evaluation of slip behaviour of self-locking modular steel
760 connection. *J Constr Steel Res* 2022;197:107467. <https://doi.org/10.1016/j.jcsr.2022.107467>.
- 761 [24] Bazarchi E, Davaran A, Lamarche CP, Roy N, Parent S. Experimental and numerical
762 investigation of a novel vertically unconstrained steel inter-modular connection. *Thin-Walled*
763 *Struct* 2023;183:110364. <https://doi.org/10.1016/j.tws.2022.110364>.
- 764 [25] Yu Y, Chen Z, Chen A. Experimental study of a pretensioned connection for modular buildings.
765 *Steel Compos Struct* 2019;31:217–32. <https://doi.org/10.12989/scs.2019.31.3.217>.
- 766 [26] Chen Z, Liu Y, Zhong X, Liu J. Rotational stiffness of inter-module connection in mid-rise
767 modular steel buildings. *Eng Struct* 2019;196:109273.
768 <https://doi.org/10.1016/j.engstruct.2019.06.009>.
- 769 [27] Wang Y, Xia J, Ma R, Xu B, Wang T. Experimental Study on the Flexural Behavior of an
770 Innovative Modular Steel Building Connection with Installed Bolts in the Columns. *Appl Sci*
771 2019;9:3468. <https://doi.org/10.3390/app9173468>.
- 772 [28] Sanches R, Mercan O, Roberts B. Experimental investigations of vertical post-tensioned
773 connection for modular steel structures. *Eng Struct* 2018;175:776–89.
774 <https://doi.org/10.1016/j.engstruct.2018.08.049>.
- 775 [29] Chen Z, Liu J, Yu Y. Experimental study on interior connections in modular steel buildings. *Eng*
776 *Struct* 2017;147:625–38. <https://doi.org/10.1016/j.engstruct.2017.06.002>.
- 777 [30] Chen Z, Wang J, Liu J, Khan K. Seismic behavior and moment transfer capacity of an innovative
778 self-locking inter-module connection for modular steel building. *Eng Struct* 2021;245:112978.
779 <https://doi.org/10.1016/j.engstruct.2021.112978>.
- 780 [31] Sanches R, Mercan O. Vertical post-tensioned connection for modular steel buildings. 12th Can.
781 Conf. Earthq. Eng. Quebec City, 2019, p. 1–8.

- 782 [32] Lee S, Park J, Shon S, Kang C. Seismic performance evaluation of the ceiling-bracket-type
783 modular joint with various bracket parameters. *J Constr Steel Res* 2018;150:298–325.
784 <https://doi.org/10.1016/j.jcsr.2018.08.008>.
- 785 [33] Deng E, Zong L, Ding Y, Dai X, Lou N, Chen Y. Monotonic and cyclic response of bolted
786 connections with welded cover plate for modular steel construction. *Eng Struct* 2018;167:407–
787 19. <https://doi.org/10.1016/j.engstruct.2018.04.028>.
- 788 [34] Chen Z, Liu J, Yu Y, Zhou C, Yan R. Experimental study of an innovative modular steel building
789 connection. *J Constr Steel Res* 2017;139:69–82. <https://doi.org/10.1016/j.jcsr.2017.09.008>.
- 790 [35] Yang C, Chen H, Ou J. Experimental study on seismic performance of modular steel construction
791 beam-to-beam combined side column joint with blind bolted connection. *Thin-Walled Struct*
792 2023;184:110431. <https://doi.org/10.1016/j.tws.2022.110431>.
- 793 [36] Annan CD, Youssef MA, Ei-Naggar MH. Effect of directly welded stringer-to-beam connections
794 on the analysis and design of modular steel building floors. *Adv Struct Eng* 2009;12:373–83.
795 <https://doi.org/10.1260/136943309788708400>.
- 796 [37] Annan CD, Youssef MA, El Naggar MH. Experimental evaluation of the seismic performance
797 of modular steel-braced frames. *Eng Struct* 2009;31:1435–46.
798 <https://doi.org/10.1016/j.engstruct.2009.02.024>.
- 799 [38] Annan CD, Youssef MA, El Naggar MH. Seismic vulnerability assessment of modular steel
800 buildings. *J Earthq Eng* 2009;13:1065–88. <https://doi.org/10.1080/13632460902933881>.
- 801 [39] Annan C, Youssef MA, Naggar MH El, Dean A. Seismic performance of modular steel braced
802 frames. *Ninth Can. Conf. Earthq. Eng. Ottawa, Ontario, Canada, 2007*.
803 <https://doi.org/10.13140/2.1.2132.2241>.
- 804 [40] Annan C, Youssef MA, Naggar MH El, Dean A. Analytical investigation of semi-rigid floor
805 beams connection in modular steel structures. *33rd Annu. Gen. Conf. Can. Soc. Civ. Eng., 2010*.
806 <https://doi.org/10.13140/2.1.2010.3687>.
- 807 [41] Liu J, Chen Z, Liu Y, Bai Y, Zhong X. Full-scale corner-supported modular steel structures with
808 vertical inter-module connections under cyclic loading. *J Build Eng* 2021;44:103269.
809 <https://doi.org/10.1016/j.jobe.2021.103269>.
- 810 [42] Liu Y, Chen Z, Liu J, Zhong X. Experimental study on seismic behavior of two-storey modular
811 structure. *Steel Compos Struct* 2020;37:273–89. <https://doi.org/10.12989/scs.2020.37.3.273>.
- 812 [43] Lacey AW, Chen W, Hao H, Bi K. Review of bolted inter-module connections in modular steel
813 buildings. *J Build Eng* 2019;23:207–19. <https://doi.org/10.1016/j.jobe.2019.01.035>.
- 814 [44] Zhao F, Yu Y, Lin S, Man M. Working mechanism evaluations and simplified models of corner
815 bracket type inter-module connections. *Struct Des Tall Spec Build* 2021;30:1–21.
816 <https://doi.org/10.1002/tal.1858>.
- 817 [45] Lacey AW, Chen W, Hao H, Bi K. Lateral behaviour of modular steel building with simplified
818 models of new inter-module connections. *Eng Struct* 2021;236:112103.
819 <https://doi.org/10.1016/j.engstruct.2021.112103>.
- 820 [46] Lyu Y, Li G, Cao K, Zhai S, Wang Y, Mao L. Bending behavior of splice connection for corner-
821 supported steel modular buildings. *Eng Struct* 2022;250:113460.
822 <https://doi.org/10.1016/j.engstruct.2021.113460>.
- 823 [47] Lyu Y, Li G, Cao K, Zhai S, Li H, Chen C, et al. Behavior of splice connection during transfer
824 of vertical load in full-scale corner-supported modular building. *Eng Struct* 2021;230:111698.
825 <https://doi.org/10.1016/j.engstruct.2020.111698>.
- 826 [48] Khan K, Chen Z, Liu J, Yan J. Simplified modelling of novel non-welded joints for modular steel
827 buildings. *Adv Steel Constr* 2021;17:412–24. <https://doi.org/10.18057/IJASC.2021.17.4.10>.
- 828 [49] Khan K, Yan J-B. Finite Element Analysis on Seismic Behaviour of Novel Joint in Prefabricated
829 Modular Steel Building. *Int J Steel Struct* 2020;20. <https://doi.org/10.1007/s13296-020-00320-w>.
830
- 831 [50] Nadeem G, Safiee NA, Abu Bakar N, Abd Karim I, Mohd Nasir NA. Finite element analysis of
832 proposed self-locking joint for modular steel structures. *Appl Sci* 2021;11.
833 <https://doi.org/10.3390/app11199277>.

- 834 [51] Chen H, Ke C, Chen C, Li G. Study on the shear behavior of inter-module connection with a bolt
835 and shear key fitting for modular steel buildings. *Adv Struct Eng* 2022;0:1–16.
836 <https://doi.org/10.1177/13694332221122547>.
- 837 [52] Ma R, Xia J, Chang H, Xu B. A component-based model for novel modular connections with
838 inbuilt component. *Appl Sci* 2021;11. <https://doi.org/10.3390/app112110503>.
- 839 [53] Hajimohammadi B, Das S, Ghaednia H, Dhanapal J. Structural performance of registration pin
840 connection in VectorBloc modular construction system. *J Constr Steel Res* 2022;197:107464.
841 <https://doi.org/10.1016/j.jcsr.2022.107464>.
- 842 [54] Pang S, Yuen J, Liew R, Dai Z. Prefabricated Prefinished Volumetric Construction Joining
843 Techniques Review. 2016 Modul. Offsite Constr. Summit Edmonton, Alberta, Canada, 2016.
844 <https://doi.org/10.29173/mocs31>.
- 845 [55] Shi F, Wang H, Zong L, Ding Y, Su J. Seismic behavior of high-rise modular steel constructions
846 with various module layouts. *J Build Eng* 2020;31:101396.
847 <https://doi.org/10.1016/j.jobe.2020.101396>.
- 848 [56] Zhang G, Xu L, Xie X. Haunch connecting techniques in a self-centering modular steel structure
849 connection system. *J Build Eng* 2022;62:105389. <https://doi.org/10.1016/j.jobe.2022.105389>.
- 850 [57] Zhang G, Xu L, Li Z. Experimental evaluation on seismic performance of a novel plug-in
851 modular steel structure connection system. *Eng Struct* 2022;273:115099.
852 <https://doi.org/10.1016/j.engstruct.2022.115099>.
- 853 [58] Deng E, Yan J, Ding Y, Zong L. Analytical and numerical studies on steel columns with novel
854 connections in Modular Construction. *Int J Steel Struct* 2017;17. <https://doi.org/10.1007/s1329>.
- 855 [59] Zhang G, Xu L, Li Z. Theoretical and parametric studies of a self-centering modular steel
856 structure connection. *Eng Struct* 2021;247:113146.
857 <https://doi.org/10.1016/j.engstruct.2021.113146>.
- 858 [60] Ma R, Xia J, Chang H, Xu B, Zhang L. Experimental and numerical investigation of mechanical
859 properties on novel modular connections with superimposed beams. *Eng Struct J* 2021;232.
860 <https://doi.org/10.1016/j.engstruct.2021.111858>.
- 861 [61] Zhang G, Xu L, Li Z. Development and seismic retrofit of an innovative modular steel structure
862 connection using symmetrical self-centering haunch braces. *Eng Struct* 2021;229:111671.
863 <https://doi.org/10.1016/j.engstruct.2020.111671>.
- 864 [62] Dai Z, Cheong TYC, Pang SD, Liew JYR. Experimental study of grouted sleeve connections
865 under bending for steel modular buildings. *Eng Struct* 2021;243:112614.
866 <https://doi.org/10.1016/j.engstruct.2021.112614>.
- 867 [63] Chen Y, Hou C, Peng J. Stability study on tenon-connected SHS and CFST columns in modular
868 construction Stability. *Steel Compos Struct* 2019;30. <https://doi.org/10.12989/scs.2019.30.2.185>.
- 869 [64] Dai Z, Pang SD, Liew JYR. Axial load resistance of grouted sleeve connection for modular
870 construction. *Thin-Walled Struct* 2020;154:106883. <https://doi.org/10.1016/j.tws.2020.106883>.
- 871 [65] Khan K, Yan J. Numerical studies on the seismic behaviour of a prefabricated multi-storey
872 modular steel building with new-type bolted joints. *Adv Steel Constr* 2021;17:1–9.
873 <https://doi.org/10.18057/IJASC.2021.17.1.1>.
- 874 [66] J. Bowron. Locating pin assembly for a modular frame.pdf. WO2020010463A1, 2020.
- 875 [67] Chen Z, Li H, Chen A, Yu Y, Wang H. Research on pretensioned modular frame test and
876 simulations. *Eng Struct* 2017;151:774–87. <https://doi.org/10.1016/j.engstruct.2017.08.019>.
- 877 [68] Peng J, Hou C, Shen L. Lateral resistance of multi-story modular buildings using tenon-
878 connected inter-module connections. *J Constr Steel Res* 2021;177:106453.
879 <https://doi.org/10.1016/j.jcsr.2020.106453>.
- 880 [69] Peng J, Hou C, Shen L. Numerical simulation of weld fracture using cohesive interface for novel
881 inter-module connections. *J Constr Steel Res* 2020;174:106302.
882 <https://doi.org/10.1016/j.jcsr.2020.106302>.
- 883 [70] Peng J, Hou C, Shen L. Progressive collapse analysis of corner-supported composite modular
884 buildings. *J Build Eng* 2022;48:103977. <https://doi.org/10.1016/j.jobe.2021.103977>.

- 885 [71] Peng J, Hou C, Shen L. Numerical analysis of corner-supported composite modular buildings
886 under wind actions. *J Constr Steel Res* 2021;187:106942.
887 <https://doi.org/10.1016/j.jcsr.2021.106942>.
- 888 [72] Liew JYR, Chua YS, Dai Z. Steel concrete composite systems for modular construction of high-
889 rise buildings. *Structures* 2019;21:135–49. <https://doi.org/10.1016/j.istruc.2019.02.010>.
- 890 [73] Liew JYR, Chua YS, Dai Z. Steel Concrete Composite Systems for Modular Construction of
891 High-rise Buildings. 12th Int. Conf. Adv. Steel-Concrete Compos. Struct. (ASCCS 2018) Univ.
892 Politècnica València, València, Spain, 2018. <https://doi.org/10.4995/ASCCS2018.2018.7220>.
- 893 [74] Khan K, Chen Z, Liu J, Javed K. State-of-the-Art on Technological Developments and
894 Adaptability of Prefabricated Industrial Steel Buildings. *Appl Sci* 2023;13.
- 895 [75] Srisangeerthan S, Hashemi MJ, Rajeev P, Gad E, Fernando S. Development of an Innovative
896 Boltless Connection for Multistory Modular Buildings. *J Struct Eng* 2022;148:1–19.
897 [https://doi.org/10.1061/\(ASCE\)ST.1943-541X.0003382](https://doi.org/10.1061/(ASCE)ST.1943-541X.0003382).
- 898 [76] Nadeem G, Azizi N, Abu N, Abd I. Experimental and numerical study of self-locking adaptable
899 inter connection for modular steel structures. *J Build Eng* 2023;65:105723.
900 <https://doi.org/10.1016/j.jobe.2022.105723>.
- 901 [77] Khan K, Chen Z, Liu J, Tsavdaridis KD, Poologanathan K. Axial compression behaviors of steel
902 shear-keyed tubular columns: Numerical and analytical studies. *J Constr Steel Res* 2023.
- 903 [78] Liu Y, Chen Z, Liu J, Zhong X, Liu X, Jiang J. Effects of various reinforcing intra-module
904 connection details on seismic behavior of corner-supported steel modular buildings. *Structures*
905 2022;40:555–70. <https://doi.org/10.1016/j.istruc.2022.04.041>.
- 906 [79] CISC. CISC Code of Standard Practice for structural steel. 2016.
- 907 [80] JGJ. Technical specification for steel structure of tall building (in Chinese). 2016.
- 908 [81] Farajian M, Sharafi P, Kildashti K. The influence of inter-module connections on the effective
909 length of columns in multi-story modular steel frames. *J Constr Steel Res* 2021;177.
910 <https://doi.org/10.1016/j.jcsr.2020.106450>.
- 911 [82] Ma R, Xia J, Chang H, Xu B, Zhang L. Experimental and numerical investigation of mechanical
912 properties on novel modular connections with superimposed beams. *Eng Struct* 2021;232.
913 <https://doi.org/10.1016/j.engstruct.2021.111858>.
- 914 [83] Xu B, Xia J, Chang H, Ma R, Zhang L. A comprehensive experimental-numerical investigation
915 on the bending response of laminated double channel beams in modular buildings. *Eng Struct*
916 2019;200. <https://doi.org/10.1016/j.engstruct.2019.109737>.
- 917 [84] Xu B, Xia J, Chang H, Ma R, Zhang L. Evaluation of superimposed bending behaviour of
918 laminated channel beams in modular steel buildings subjected to lateral load. *Thin-Walled Struct*
919 *J* 2022;175. <https://doi.org/10.1016/j.tws.2022.109234>.
- 920 [85] Wang Q, Su M. Stability study on sway modular steel structures with semi-rigid connections.
921 *Thin-Walled Struct* 2021;161. <https://doi.org/10.1016/j.tws.2021.107529>.
- 922 [86] Khan K, Chen Z, Liu J, Khan A, Javed K. Axial compression behaviours of tubular sectioned C-
923 shape continuous-supported steel walls in MSB. *J Constr Steel Res* 2022;188:107009.
924 <https://doi.org/10.1016/j.jcsr.2021.107009>.
- 925 [87] Khan K, Chen Z, Liu J, Khan A. Experimental and numerical study on planar multi-column walls
926 behaviours with boundary supports. *J Constr Steel Res* 2021;186:106880.
927 <https://doi.org/10.1016/j.jcsr.2021.106880>.
- 928 [88] Khan K, Chen Z, Liu J, Khan A. Numerical and parametric analysis on compressive behaviours
929 of continuous-supported wall systems in MSB. *Structures* 2021;33:4053–79.
930 <https://doi.org/10.1016/j.istruc.2021.07.001>.
- 931 [89] Hou J, Wang X, Liu J, Chen Z, Zhong X. Study on the stability bearing capacity of multi-column
932 wall in modular steel building. *Eng Struct* 2020;214:110648.
933 <https://doi.org/10.1016/j.engstruct.2020.110648>.
- 934 [90] Mark Lawson R, Richards J. Modular design for high-rise buildings. *Proc Inst Civ Eng Struct*
935 *Build* 2010;163:151–64. <https://doi.org/10.1680/stbu.2010.163.3.151>.

- 936 [91] Khan K, Chen Z, Liu J, Javed K. Compressive behaviors of modular steel shear-keyed grouped
937 tubular columns. *J Build Eng* 2023;66:105861. <https://doi.org/10.1016/j.jobe.2023.105861>.
- 938 [92] Khan K, Chen Z, Liu J, Javed K. Experimental and analytical investigations on compressive
939 behaviors of modular steel shear-keyed tubes. *Eng Struct* 2023;279:115604.
940 <https://doi.org/10.1016/j.engstruct.2023.115604>.
- 941 [93] Pengfei Z, Xizhi Z, Zhihua C, Tianxin Z. Design and Mechanical Properties of Multi-storey Steel
942 Module Structure (in Chinese). Tianjin University, 2015.
- 943 [94] Dhanapal J, Ghaednia H, Das S, Velocci J. Structural performance of state-of-the-art VectorBloc
944 modular connector under axial loads. *Eng Struct* 2019;183:496–509.
945 <https://doi.org/10.1016/j.engstruct.2019.01.023>.
- 946 [95] Deng E, Lian J, Zhang Z, Qian H, Zhang G, Zhang P. Axial mechanical behavior of an innovative
947 liftable connection for modular steel construction. *Thin-Walled Struct* 2023;182:110256.
948 <https://doi.org/10.1016/j.tws.2022.110256>.
- 949 [96] Deng EF, Lian JY, Liu Z, Zhang GC, Wang SB, Cao D Bin. Compressive Behavior of a Fully
950 Prefabricated Liftable Connection for Modular Steel Construction. *Buildings* 2022;12.
951 <https://doi.org/10.3390/buildings12050649>.
- 952 [97] Wang Q, Su M. Stability study on sway modular steel structures with semi-rigid connections.
953 *Thin-Walled Struct* 2021;161:107529. <https://doi.org/10.1016/j.tws.2021.107529>.
- 954 [98] Li GQ, Cao K, Lu Y, Jiang J. Effective length factor of columns in non-sway modular steel
955 buildings. *Adv Steel Constr* 2017;13:412–26. <https://doi.org/10.18057/IJASC.2017.13.4.6>.
- 956 [99] Li GQ, Cao K, Lu Y. Column effective lengths in sway-permitted modular steel-frame buildings.
957 *Proc Inst Civ Eng Struct Build* 2019;172:30–41. <https://doi.org/10.1680/jstbu.17.00006>.
- 958 [100] Zhai X, Zha X, Chen D. Elastic stability of unbraced plate-type modular steel frames with semi-
959 rigid corner connections. *J Constr Steel Res* 2022;192:107243.
960 <https://doi.org/10.1016/j.jcsr.2022.107243>.
- 961 [101] Wang Q, Su M. Stability study on sway modular steel structures with semi-rigid connections.
962 *Thin-Walled Struct* 2021;161:107529. <https://doi.org/10.1016/j.tws.2021.107529>.
- 963 [102] Dumonteil P. Simple Equations for Effective Length Factors. *Am Inst Steel Constr* 1992;Vol.
964 29:111–5.
- 965 [103] He XHC, Chan TM. Classification system for inter- and intra-module joints in non-sway steel
966 MiC structures. *J Constr Steel Res* 2023;206:107913. <https://doi.org/10.1016/j.jcsr.2023.107913>.
- 967 [104] Farajian M, Sharafi P, Eslamnia H, Bai Y, Samali B. Classification system for inter-modular
968 connections in non-sway corner-supported steel modular buildings. *Structures* 2023;49:807–25.
969 <https://doi.org/10.1016/j.istruc.2023.01.152>.
- 970 [105] Farajian M, Sharafi P, Eslamnia H, Kildashti K, Bai Y. Classification of inter-modular
971 connections for stiffness and strength in sway corner-supported steel modular frames. *J Constr*
972 *Steel Res* 2022;107458.
- 973 [106] Chen Z, Zhong X, Liu Y, Liu J. Analytical and Design Method for the Global Stability of
974 Modular Steel Buildings. *Int J Steel Struct* 2021;21:1741–58. <https://doi.org/10.1007/s13296-021-00532-8>.
- 976 [107] Fathieh A, Mercan O. Seismic evaluation of modular steel buildings. *Eng Struct* 2016;122:83–
977 92. <https://doi.org/10.1016/j.engstruct.2016.04.054>.
- 978 [108] Yu Y, Chen Z. Rigidity of corrugated plate sidewalls and its effect on the modular structural
979 design. *Eng Struct* 2018;175:191–200. <https://doi.org/10.1016/j.engstruct.2018.08.039>.
- 980 [109] Lee S, Park J, Kwak E, Shon S, Kang C, Choi H. Verification of the seismic performance of a
981 rigidly connected modular system depending on the shape and size of the ceiling bracket.
982 *Materials (Basel)* 2017;10. <https://doi.org/10.3390/ma10030263>.
- 983 [110] L D, Chen W-F. Effective length factor for columns in braced frames. *J Struct Eng*
984 1989;114:2357–70.
- 985 [111] L. Duan, Chen W-F. Effective length factor for columns in unbraced frames. *J Struct Eng*
986 1989;115:149–65.

- 987 [112] Sharafi P, Mortazavi M, Samali B, Ronagh H. Interlocking system for enhancing the integrity of
988 multi-storey modular buildings. *Autom Constr* 2018;85:263–72.
989 <https://doi.org/10.1016/j.autcon.2017.10.023>.
- 990 [113] Chen Z, Zhou Z, Liu J, Ren J, Du E. A kind of corner rotary modular building connection node
991 (in Chinese). CN 106149901 A, 2016.
- 992 [114] Xianfeng Li. Tianjin Ziya Shanglinyuan, the first formally approved modular residential project
993 in China (in Chinese). *Build Assem Build Netw* 2017.
994 https://www.sohu.com/a/143163457_714527.
- 995 [115] GB50017-2017. Standard for design of steel structures (in Chinese) 2017.
- 996 [116] Zhong X, Chen Z, Liu J, Liu Y, Liu X. Experimental research on the in-plane performance of
997 discontinuous modular diaphragms. *Thin-Walled Struct* 2022;173:108905.
998 <https://doi.org/10.1016/j.tws.2022.108905>.
- 999 [117] GB/T 228.1-2010. Metallic materials-Tensile testing-Part 1: Method of test at room temperature
1000 (in Chinese) 2010.
- 1001 [118] Liu Y, Chen Z, Liu J, Zhong X, Liu X, Jiang J. Effects of various reinforcing intra-module
1002 connection details on seismic behavior of corner-supported steel modular buildings. *Structures*
1003 2022;40:555–70. <https://doi.org/10.1016/j.istruc.2022.04.041>.
- 1004 [119] GBT50344-2019. Technical standards for building structure inspection (in Chinese) 2019.
- 1005 [120] Sun M, Qu G, Geng L, Hou D, Jing S. Fatigue Properties and Damage Characteristics of
1006 Polyurethane Mixtures under a Stress Control Mode. *Sustain* 2022;14.
1007 <https://doi.org/10.3390/su141710966>.
- 1008 [121] Wangxi Z. "Structural Testing" (Part of the Higher Education Civil Engineering Major Excellent
1009 Engineer Education and Training Program Series Planning Textbook)- in Chinese. vol. 2016. 1st
1010 ed. Wuhan University Press; 2016.
- 1011 [122] Yu Y, Lan L, Chen Z, Huang J. Mechanical and seismic behaviors of bottom-flange-bolted
1012 upper-flange-welded through-diaphragm connections. *J Constr Steel Res* 2019;156:86–95.
1013 <https://doi.org/10.1016/j.jcsr.2019.01.015>.
- 1014 [123] Yan JB, Dong X, Zhu JS. Behaviours of stub steel tubular columns subjected to axial
1015 compression at low temperatures. *Constr Build Mater* 2019;228:116788.
1016 <https://doi.org/10.1016/j.conbuildmat.2019.116788>.
- 1017 [124] Kang SB, Yang B, Zhou X, Nie SD. Global buckling behaviour of welded Q460GJ steel box
1018 columns under axial compression. *J Constr Steel Res* 2018;140:153–62.
1019 <https://doi.org/10.1016/j.jcsr.2017.10.013>.
- 1020 [125] Kazemzadeh Azad S, Li D, Uy B. Axial slenderness limits for duplex and lean duplex stainless
1021 steel-concrete composite columns. *J Constr Steel Res* 2020;172:106175.
1022 <https://doi.org/10.1016/j.jcsr.2020.106175>.
- 1023 [126] Yan J, Zhang B, Yu X, Xie J. Thin-Walled Structures Mechanical properties of stainless steel
1024 QN1906Mo at sub-zero temperatures: Tests and stress – strain models. *Thin-Walled Struct*
1025 2022;179:109727. <https://doi.org/10.1016/j.tws.2022.109727>.
- 1026 [127] Yan JB, Luo YL, Liang C, Lin X, Luo YB, Zhang L. Compression behaviours of concrete-filled
1027 Q690 high-strength steel tubular columns at low temperatures. *J Constr Steel Res*
1028 2021;187:106983. <https://doi.org/10.1016/j.jcsr.2021.106983>.
- 1029 [128] Yan JB, Yang X, Luo Y, Xie P, Luo YB. Axial compression behaviours of ultra-high
1030 performance concrete-filled Q690 high-strength steel tubes at low temperatures. *Thin-Walled*
1031 *Struct* 2021;169:108419. <https://doi.org/10.1016/j.tws.2021.108419>.
- 1032 [129] Yan JB, Wang T, Dong X. Compressive behaviours of circular concrete-filled steel tubes
1033 exposed to low-temperature environment. *Constr Build Mater* 2020;245:118460.
1034 <https://doi.org/10.1016/j.conbuildmat.2020.118460>.
- 1035 [130] Yan JB, Xie WJ, Luo Y, Wang T. Behaviours of concrete stub columns confined by steel tubes
1036 at cold-region low temperatures. *J Constr Steel Res* 2020;170:106124.
1037 <https://doi.org/10.1016/j.jcsr.2020.106124>.

- 1038 [131] Yan JB, Dong X, Wang T. Axial compressive behaviours of square CFST stub columns at low
1039 temperatures. *J Constr Steel Res* 2020;164:105812. <https://doi.org/10.1016/j.jcsr.2019.105812>.
- 1040 [132] Yan JB, Luo YL, Su L, Lin X, Luo YB, Zhang L. Low-temperature compression behaviour of
1041 square CFST columns using Q960 ultra-high strength steel. *J Constr Steel Res* 2021;183.
1042 <https://doi.org/10.1016/j.jcsr.2021.106727>.
- 1043 [133] Du Y, Fu M, Chen Z, Yan J, Zheng Z. Axial compressive behavior of CFRP confined rectangular
1044 CFT columns using high-strength materials : Numerical analysis and carrying capacity model.
1045 *Structures* 2022;36:997–1020. <https://doi.org/10.1016/j.istruc.2021.12.061>.
- 1046 [134] Yan J, Feng J, Luo Y, Du Y. Compression behaviour of stainless-steel stub square tubular
1047 columns at cold-region low temperatures. *J Constr Steel Res* 2021;187:106984.
1048 <https://doi.org/10.1016/j.jcsr.2021.106984>.
- 1049 [135] ABAQUS (2013). User manual Version 6.13. DS SIMULIA Corp, Provid RI, USA 2013:1–847.
- 1050 [136] Jia L, Zhao Y, Liu H, Chen Z, Kashan K. Flexural performance of weld-strengthened steel beam-
1051 square column joints subjected to axial column loading. *J Constr Steel Res* 2022;199:107599.
1052 <https://doi.org/10.1016/j.jcsr.2022.107599>.
- 1053 [137] Gardner L, Saari N, Wang F. Comparative experimental study of hot-rolled and cold-formed
1054 rectangular hollow sections. *Thin-Walled Struct* 2010;48:495–507.
1055 <https://doi.org/10.1016/j.tws.2010.02.003>.
- 1056 [138] Arrayago I, Rasmussen KJR. Influence of the imperfection direction on the ultimate response of
1057 steel frames in advanced analysis. *J Constr Steel Res* 2022;190:107137.
1058 <https://doi.org/10.1016/j.jcsr.2022.107137>.
- 1059 [139] Theofanous M, Gardner L. Testing and numerical modelling of lean duplex stainless steel hollow
1060 section columns. *Eng Struct* 2009;31:3047–58. <https://doi.org/10.1016/j.engstruct.2009.08.004>.
- 1061 [140] Yan JB, Geng Y, Luo Y, Zhao B, Wang T. Double skin composite beams at Arctic low
1062 temperatures: Numerical and analytical studies. *J Constr Steel Res* 2022;193:107286.
1063 <https://doi.org/10.1016/j.jcsr.2022.107286>.
- 1064 [141] Yan JB, Dong X, Zhu JS. Behaviours of stub steel tubular columns subjected to axial
1065 compression at low temperatures. *Constr Build Mater* 2019;228.
1066 <https://doi.org/10.1016/j.conbuildmat.2019.116788>.
- 1067 [142] Yan JB, Feng J, Luo YB, Du Y. Compression behaviour of stainless-steel stub square tubular
1068 columns at cold-region low temperatures. *J Constr Steel Res* 2021;187:106984.
1069 <https://doi.org/10.1016/j.jcsr.2021.106984>.
- 1070 [143] Zhu J-H, Young B. Cold-Formed-Steel Oval Hollow Sections under Axial Compression. *J Struct*
1071 *Eng* 2011;137:719–27. [https://doi.org/10.1061/\(asce\)st.1943-541x.0000337](https://doi.org/10.1061/(asce)st.1943-541x.0000337).
- 1072 [144] Dabaon MA, El-Boghdadi MH, Hassanein MF. A comparative experimental study between
1073 stiffened and unstiffened stainless steel hollow tubular stub columns. *Thin-Walled Struct*
1074 2009;47:73–81. <https://doi.org/10.1016/j.tws.2008.05.008>.
- 1075 [145] IS 801 - 1975. Indian Standard code of practice for use of cold-formed light gauge steel structural
1076 members in general building construction 1975.
- 1077 [146] IS:800. Indian standard code of practice for general construction in steel. Bur Indian Stand New
1078 Delhi 2007.
- 1079 [147] NZS3404. Part 1:1997-Steel Structures Standard 1997.
- 1080 [148] EN 1993-1-1. Eurocode 3: Design of steel structures - Part 1-1: General rules and rules for
1081 buildings. vol. 1. 2005.
- 1082 [149] CSA-S16-09. CSA standard-Design of steel structures. vol. 7. 2009.
- 1083 [150] ANSI/AISC 360-16. AISC360/16 Specification for Structural Steel Buildings-An American
1084 National Standard. 2016.
- 1085 [151] Chen Y, Hou C, Peng J. Stability study on tenon-connected SHS and CFST columns in modular
1086 construction. *Steel Compos Struct* 2019;30:185–99. <https://doi.org/10.12989/scs.2019.30.2.185>.
- 1087 [152] Chen WF, Lui EM. Stability design of steel frames. vol. 53. CRC Press; 1991.

